Journal of Materials Chemistry A

ROYAL SOCIETY OF CHEMISTRY

REVIEW

View Article Online
View Journal | View Issue

Cite this: J. Mater. Chem. A, 2023, 11, 5476

Manganese-based oxide electrocatalysts for the oxygen evolution reaction: a review

Peng Wang,[ab] Shiqi Zhang,[ab] Zhaobo Wang,[ab] Yuhan Mo,[ab] Xiaoyang Luo,[ab] Fan Yang,[c] Meili Lv,[c] Zhaoxiang Li[d] and Xuanwen Liu *[a]

Received 20th November 2022
Accepted 13th February 2023

DOI: 10.1039/d2ta09039b

rsc.li/materials-a

The oxygen evolution reaction (OER), as an essential process in water decomposition and air batteries, has received increasing attention in the context of clean energy production and efficient energy storage. With their abundant composition and morphology, manganese-based oxides (MnO_x) offer great possibilities for the exploration and design of OER catalysts. In this paper, three classes of MnO_x materials, including MnO_2, Mn_2O_3, and Mn_3O_4, are systematically reviewed and their development and applications in OER systems are comprehensively presented. Subsequently, the effects of Jahn–Teller distortion and the question of the active site and stability of MnO_x in the OER are discussed, and the presence of Mn^{3+}, which is considered essential for OER activity, and strategies for improving performance are proposed. This paper focuses on the impact of crystal structure, catalytic mechanisms, and design strategies on MnO_x.

1. Introduction

The energy crisis caused by the exploitation and overconsumption of fossil fuels and the increasingly severe climate change have emerged as two prominent issues constraining human development.[1–3] Hydrogen can replace fossil fuels as the main energy source, and improving hydrogen production by electrolysis of water is one of the most promising sustainable methods. Nevertheless, the development of hydrogen evolution in water electrolysis is limited by the anodic oxygen evolution reaction (OER) as a consequence of its moderate multi-electron transfer process. The most commonly used electrocatalysts for the OER are noble metals and their oxides, such as Ir, Ru, IrO_2, and RuO_2, but their extreme cost and scarcity prevent their large-scale application. Therefore, the development of oxygen-evolving electrocatalysts with excellent catalytic properties, elevated stability, and low cost is essential.[4–7] Thus far, transition metal matrices (Fe, Co, *etc.*) and transition metal oxides, nitrides, carbides, hydroxides, and sulfides have been proven to have elevated catalytic activity in the field of water electrolysis.[8–11]

Manganese-based oxides (MnO_x) are attractive materials in various fields due to their low price, natural abundance, and low toxicity. With its wide range of oxidation states, MnO_x can be broadly classified as MnO_2 (oxidation state of +4), Mn_3O_4 (mixed state), Mn_2O_3 (oxidation state of +3), and MnO (oxidation state of +2).[12] Take the most common MnO_2, for example, there are six crystal structures of MnO_2, which means that MnO_2 can be prepared by adjusting its preparation method to obtain catalysts with different surface areas and controllable morphology, and it is found that the conversion between different crystal structures of MnO_2 will improve its catalytic performance.[13] However, there are still insufficient studies on MnO_x in the OER direction. The catalytic activity of MnO_x is extremely different from that of iron, cobalt, and nickel catalysts, whose limited active sites and low conductivity limit their development. Therefore, it is necessary to explore its catalytic properties in-depth and implement modification strategies such as defect engineering or heteroatom incorporation.[14]

Based on the current research progress, the conventional adsorption mechanism of the OER in an alkaline environment is first discussed in this paper. Second, the latest research progress of MnO_x (MnO_2, Mn_3O_4, and Mn_2O_3) as OER catalysts is reviewed. Of these MnO_x materials, MnO_2 is currently the most well studied, followed by Mn_3O_4 and Mn_2O_3. After that, the Jahn–Teller distortion, active sites, and stability issues in MnO_x catalysts and suggested ways to improve OER activity, including the introduction of vacancies and the formation of heterogeneous interfaces are discussed. We believe that this review can serve as a reference for the development of high-quality manganese oxide catalysts.

2. The OER mechanism

The reaction mechanism of the OER is thought to be through two possible pathways: the adsorption evolution mechanism

[a]School of Materials Science and Engineering, Northeastern University, Shenyang 110819, PR China. E-mail: lxw@neuq.edu.cn

[b]Key Laboratory of Dielectric and Electrolyte Functional Material Hebei Province, School of Resources and Materials, Northeastern University at Qinhuangdao, Qinhuangdao 066004, PR China

[c]Qinhuangdao Solid Waste Management Centre, Qinhuangdao 066004, PR China

[d]Qinhuangdao Capital Starlight Environmental Technology Co., Ltd, Qinhuangdao 066004, PR China

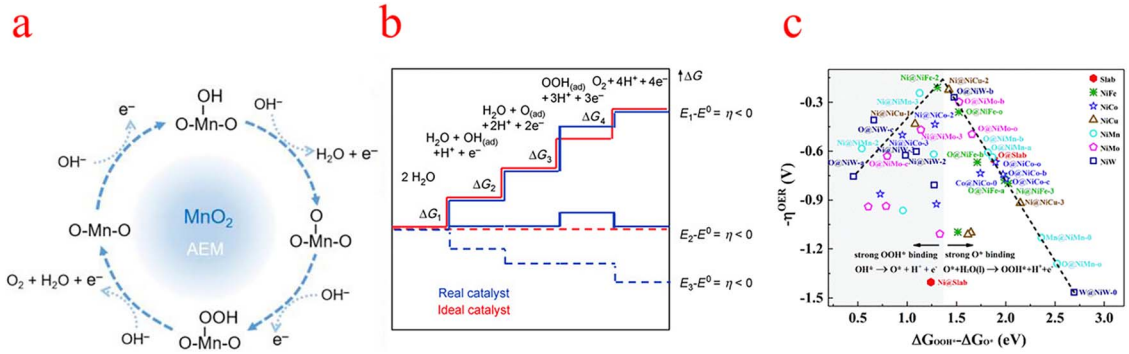

Fig. 1 (a) Schematic diagram of the OER mechanism indicated (using MnO_2 as an example). (b) Gibbs free energy and reaction coordinate diagram of active intermediates (horizontal line) of the OER. The blue line and red line represent the real (typical) catalyst and the ideal catalyst respectively. (c) Overpotential ($-\eta^{OER}$) Gibbs free binding energy difference with different reaction sites OOH* and O*. (a) Reproduced with permission from ref. 17. Copyright 2023, American Chemical Society. (b) Reproduced with permission from ref. 25. Copyright 2010, John Wiley and Sons. (c) Reproduced with permission from ref. 30. Copyright 2019, Royal Society of Chemistry.

(AEM) and lattice oxygen mechanism (LOM).[15] The AEM is a more general mechanism for OER catalysts (Fig. 1a), and the LOM normally occurs in extremely covalent oxides.[4,16,17] In this section, we focus on the proportionality of AEM to different reaction intermediates. The AEM pathway is a four-coordinated proton-electron transfer reaction centered on metal ions, as shown in eqn (1)–(4).[18] MOH, MO, and MOOH represent intermediates adsorbed on active sites. The hydroxy anion (OH^-) is first adsorbed on the surface of the metal site (M) through the single electron oxidation process, forming adsorbed MOH at the M site. Then, MOH intermediates are oxidized to form MO substances. The subsequent O–O bond formation step is usually considered the rate-determining step for most catalysts in this step where MO reacts with another OH^- to form MOOH. Finally, MOOH is oxidized by a single electron transfer process, releasing O_2 and restoring the original M active site.[19]

$$OH^- + M \rightarrow MOH + e^- (\Delta G_1) \quad (1)$$

$$MOH + OH^- \rightarrow MO + H_2O + e^- (\Delta G_2) \quad (2)$$

$$MO + OH^- \rightarrow MOOH + e^- (\Delta G_3) \quad (3)$$

$$MOOH + OH^- \rightarrow O_2 + M + H_2O + e^- (\Delta G_4) \quad (4)$$

The Gibbs free energy variation of the above four-electron transfer process can be calculated using the following eqn (5)–(8).[20,21]

$$\Delta G_1 = G_{MOH} - G_M - (G_{OH^-} - G_{e^-}) \quad (5)$$

$$\Delta G_2 = G_{MO} + G_{H_2O(l)} - G_{MOH} - (G_{OH^-} - G_{e^-}) \quad (6)$$

$$\Delta G_3 = G_{MOOH} - G_{MO} - (G_{OH^-} - G_{e^-}) \quad (7)$$

$$\Delta G_4 = G_M + G_{O_2}(g) + G_{H_2O(l)} - G_{MOOH} - (G_{OH^-} - G_{e^-}) \quad (8)$$

Each elementary step has the specific free energy of the corresponding intermediate. The step with the maximum free energy difference ($G = \mathrm{Max}[\Delta G_1, \Delta G_2, \Delta G_3, \Delta G_4]$) is identified as the rate-determining step and the theoretical overpotential of the overall reaction ($\eta = (G/e) - 1.23$ V).[22] Specifically, catalytic activity is estimated from the magnitude of the potential determining step G^{OER} of the OER.[23] That is to say, all adsorption intermediates of MOH, MO, and MOOH should balance the fracture of the O–M bond and the formation of the O–O bond to ensure that the bonding strength of O–M is neither too strong nor too weak.[24] An ideal catalyst in thermodynamics requires that all four steps have the same order of reaction-free energy as shown in the figure (Fig. 1b).[25] Under this condition, all reaction-free energies are zero at the equilibrium potential (1.23 V), if ignoring the desorption step. Given the constant adsorption energy difference between MOH and MOOH ($\Delta G_{MOOH} = \Delta G_{MOH} + 3.2 \pm 0.2$ eV), OER overpotential can be determined from MO adsorption energy, which means that the second or third process is the decisive step. According to Sabatier's principle, the ideal catalyst requires that the adsorption strength of key intermediates is neither too strong nor too weak.[26–28] As such, η^{OER} as ($\Delta G_{MO} - \Delta G_{MOH}$) leads to a universal volcanic shape relationship (Fig. 1c); an ideal OER electrocatalyst with optimum activity requires an intermediate binding strength and an $\Delta G_{MO} - \Delta G_{MOH}$ value of 1.6 eV (corresponding to the peak of the volcano).[29–31]

Although the electrocatalytic decomposition of water has been studied since the last century and the basic mechanism of the anodic OER has been revealed, there are still different debates on the mechanism of water decomposition.[32,33] Understanding the underlying mechanisms can only help us to find the source of active sites for different materials and to bring the catalyst performance close to the theoretical thermodynamic limit, which contributes to the understanding of the necessary reactions of MnO_x in the OER process. In the following subsections, we focus on MnO_x electrocatalysts with different crystal structures and their impact on electrochemical properties.

3. Application of manganese-based oxides in the OER

The oxygen-evolving complex (OEC) of photosystem II uses catalytic Mn_4CaO_n clusters to generate molecular oxygen from water. It is inspired by this MnO_x catalyst that is receiving more and more attention.[34,35] Preliminary studies have shown that manganese oxides enhance water oxidation due to their elevated thermodynamic stability, suitability of specific surface areas, and oxidation enthalpy.[36,37] Moreover, with the introduction of additional characterization techniques and the development of electrochemistry, more stable and efficient materials have been designed and synthesized to improve the catalytic performance of MnO_x. Recent advances in MnO_x as an OER electrode material are discussed in detail in this section.

3.1 MnO_2

MnO_2 and its composites have been widely used in supercapacitor and battery applications due to their low cost, environmentally friendly nature, high operating voltage, and theoretical capacity. Notably, MnO_2 exists in a variety of crystalline polycrystalline forms, such as α-MnO_2, β-MnO_2, γ-MnO_2, and δ-MnO_2 (Fig. 2), and the crystal structure is diversified and controllable.[38–40] The MnO_2 crystal consists of [MnO_6] octahedral units with oxygen atoms at the top of the six corners of the octahedron and manganese atoms in the center. These octahedral units are connected by common corners or edges, resulting in the formation of various tunneling and layered structures. MnO_2 crystals (α-MnO_2, β-MnO_2, γ-MnO_2, and δ-MnO_2) can be classified into three categories: a one-dimensional tunneling structure, a two-dimensional layered structure (δ-MnO_2), and a three-dimensional network structure formed by the common sides of [MnO_6] octahedra λ-MnO_2.[41,42] As a consequence of the multivalent state of Mn and a large number of crystalline phases, MnO_2 invariably contains impurities from multiple polycrystalline phases, a complex structure–property relation.[43] Different crystalline phases significantly affect the catalytic properties of MnO_2 and, in particular, the crystal structure of MnO_2 plays a key role in determining the catalytic properties. The OER activity is reported to follow the order α-MnO_2 > β-MnO_2 > δ-MnO_2.[44,45] What follows is an elaboration of the physical and chemical properties of MnO_2 electrocatalysts with different crystalline phases in terms of catalytic activity, electron/ion conductivity, and electrochemical properties.

3.1.1 α-MnO_2. α-MnO_2 has a one-dimensional 2 × 2 (0.46 × 0.46 nm^2) tunnel structure, which acts as a channel for ions and molecules. The presence of water and cations in the α-MnO_2 crystal structure acts as a support tunnel, otherwise, the structure would collapse and transform into another crystal, β-MnO_2, which is the most intuitive difference between the two

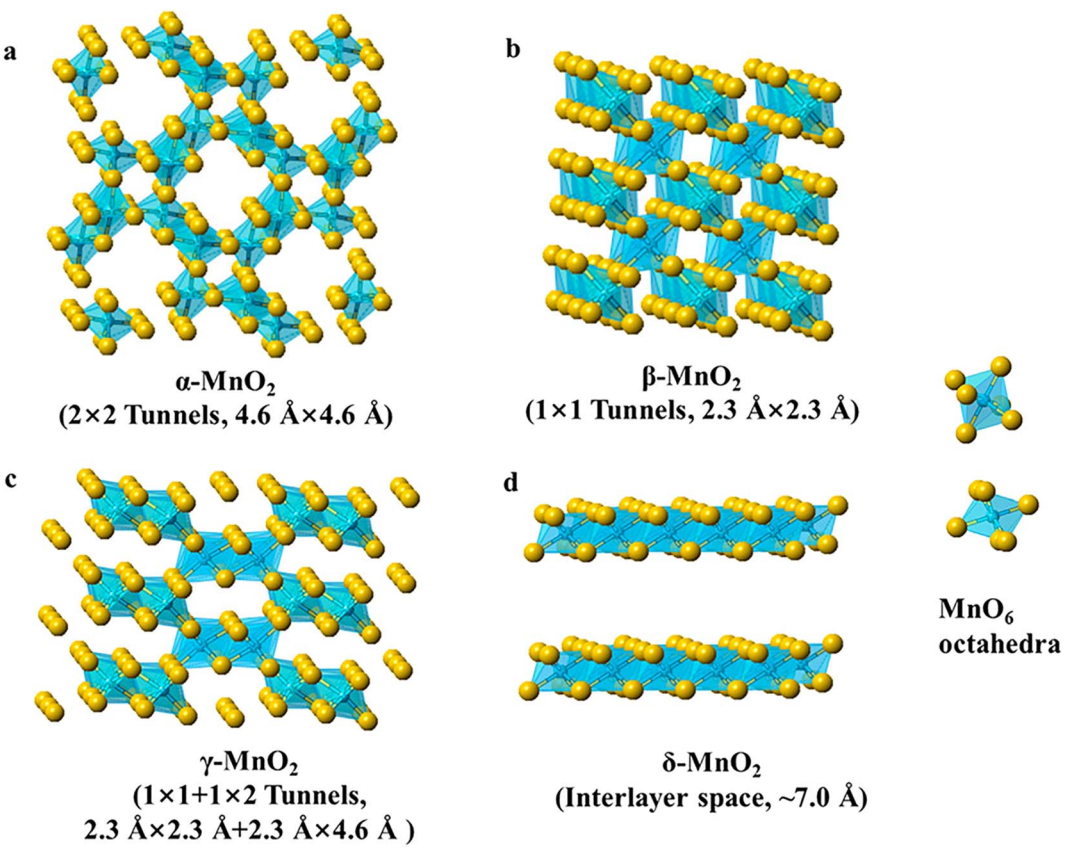

Fig. 2 Polyhedral representation of several manganese oxide crystals (α-MnO_2, β-MnO_2, γ-MnO_2, and δ-MnO_2). Reproduced with permission from ref. 40. Copyright 2019, American Chemical Society.

crystal structures.[46] Manganese centers are mixed valence (+3 and +4), where charge neutrality can be maintained by cations within the tunnel structure.[47] In addition, the tunnel space in α-MnO_2 can also alleviate the strain induced by the ion insertion/desorption process, so that α-MnO_2 has excellent structural stability.[48] Extensive characterization shows that the OER catalytic performance of MnO_2 is greatly dependent on the crystal structure and follows the order of α-MnO_2 > β-MnO_2 > δ-MnO_2, as shown in Fig. 3a. This is due to the existence of α-MnO_2 active sites in the edge-shared [MnO_6] unit, the suitable tunnel size, large surface area providing high accessibility to water molecules, existence of a large number of di-μ-oxo bridges as protonation sites in α-MnO_2 and the mixed valence of Mn (AOS = 3.7); at the same time, *in situ* electrochemical impedance spectroscopy (EIS) showed the smallest charge transfer resistance compared with alternative crystal forms of MnO_2.[45]

Gu used ionic liquids (ILs) as a structural inducer to transform the crystalline structure and morphology of the reaction product from β-MnO_2 nanorods to α-MnO_2 nanowires with a high specific surface area (Fig. 3b), and X-ray absorption near edge structure (EXANES) and X-ray photoelectron spectroscopy (XPS) analyses show that the transformed α-MnO_2 has a high Mn III content and an abundance of oxygen vacancies, which is beneficial for the OER. At 10 mA cm^{-2}, the overpotential is 394 mV and the Tafel slope is low at 49 mV $\cdot dec^{-1}$. Also, Gu's research has shown that the crystal structure has a much more decisive and critical influence on the catalytic OER than the surface area.[49] Subsequently, Zhou's group similarly used the structural transformation of MnO_2 to induce its phase transition from δ to α by merely adjusting the hydrothermal time (Fig. 3c). The transformed α-MnO_2 has nanowire and nanosheet morphologies that expand the specific surface area and thus expose more catalytically active sites; the higher content of Mn III ions and oxygen vacancies detected by XPS and electron paramagnetic resonance (EPR) will contribute to better catalytic performance; and density functional theory (DFT) calculations show that α-MnO_2 has a more suitable energy band gap (which leads to better electron conductivity and transfer).[50] Ni *et al.* reported that single-atom Ag-doped MnO_2 nanowires can catalyze both the OER and oxygen reduction reaction (ORR), due to the strong Ag–O bond weakening the surrounding Mn–O bond, leading to significant crystal distortion, which likely favorably modulates the binding energy of the reaction intermediates, resulting in higher activity. Moreover, the synergistic effect of Ag and MnO_2 should enhance the electrocatalytic activity, and the metallic and transition metal oxides modify the electronic

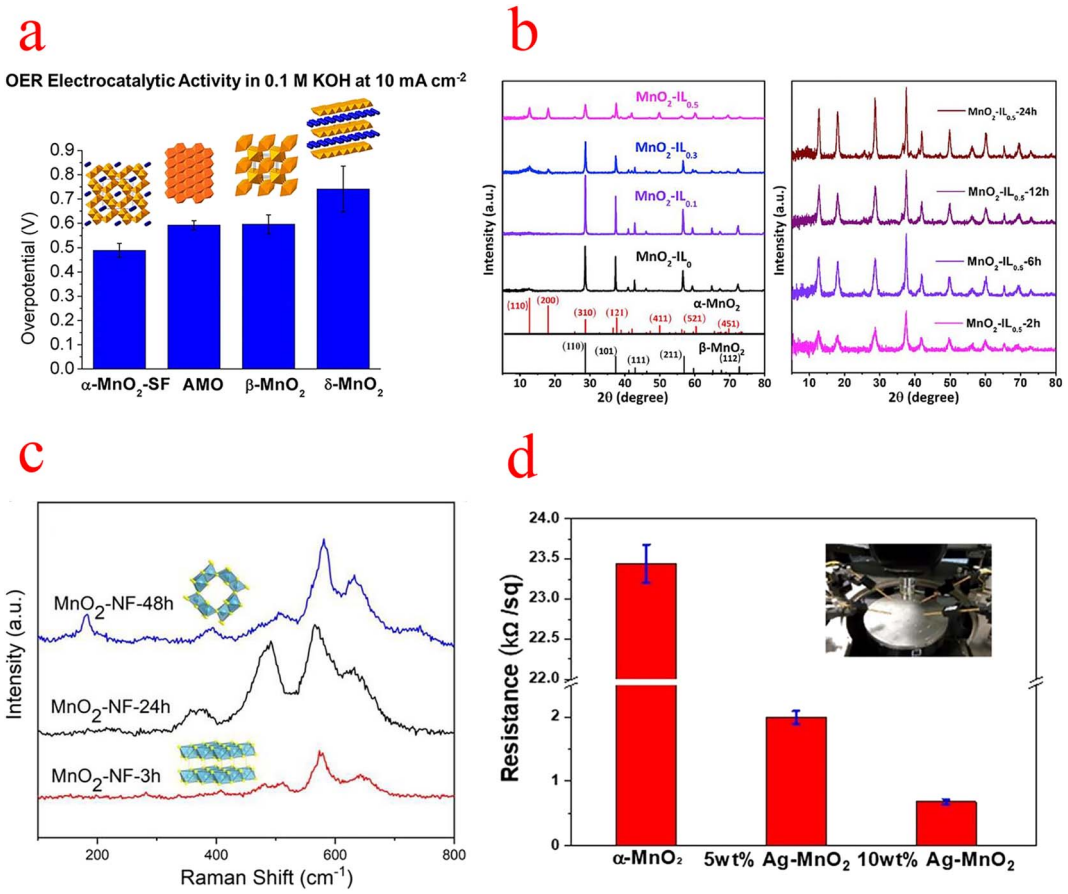

Fig. 3 (a) Comparison of the overpotential of MnO_2 at 10 mA cm^{-2}. (b) XRD patterns of MnO_2 with different IL additions and different reaction times. (c) Raman spectra of MnO_2–NF at different hydrothermal times. (d) Resistivity measurements of several types of MnO_2. (a) Reproduced with permission from ref. 45. Copyright 2014, American Chemical Society. (b) Reproduced with permission from ref. 49. Copyright 2019, Elsevier. (c) Reproduced with permission from ref. 50. Copyright 2019, Elsevier. (d) Reproduced with permission from ref. 51. Copyright 2019, Elsevier.

structure of the metal and induce a shift of the d-band center. XPS studies confirm that Ag doping produces a large number of surface oxygen vacancies, which open the octahedral walls of MnO_2 and facilitate ion diffusion. And the resistivity of α-MnO_2 was also measured with a four-point probe, which decreased by more than 20 times after Ag doping (Fig. 3d).[51]

3.1.2 β-MnO_2. β-MnO_2 uses a 1 × 1 tunnel structure consisting of corner connected [MnO_6] octahedral chains. Among the various polymorphisms of MnO_2, β-MnO_2 has long been considered an inert electrocatalyst for oxygen conversion due to its elevated thermodynamic stability and perfect lattice structure.[52] Although both β-MnO_2 and α-MnO_2 have tunnel structures, it has much lower OER activity, and this difference in activity is related to their structures. β-MnO_2 has the smallest BET surface area and porosity due to its small tunnel size, which cannot accommodate any cations, and its crystal structure has the highest Mn^{4+} content. Comparatively, α-MnO_2 has a larger tunnel structure to accommodate cations (K^+) and water, and therefore has a much higher BET surface area and porosity; more importantly, α-MnO_2 has mixed valence (Mn^{3+}/Mn^{4+}) in it,

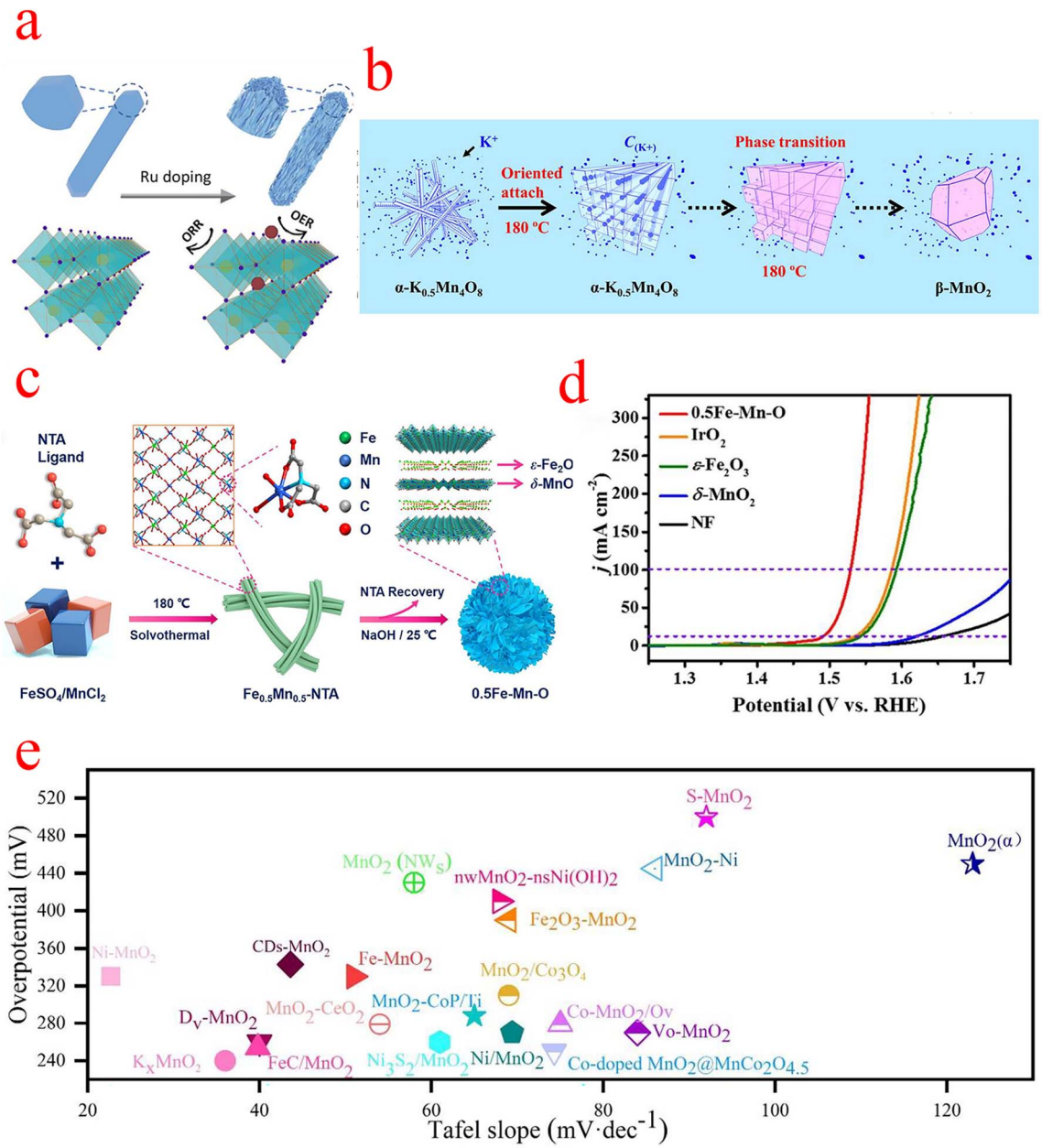

Fig. 4 (a) Schematic diagram of Ru doping-induced crystal splitting of β-MnO_2 and its OER and ORR sites. (b) The schematic diagram illustrates the directional attachment and phase transformation process. During the phase transition, K^+ stable cations are expelled from the crystal structure. (c) Schematic diagram of the synthesis of 0.5Fe–Mn–O nanosheets. (d) Linear sweep voltammetry (LSV) in 1 M KOH aqueous solution. (e) Overpotential and Tafel slope of MnO_2 compounded OER electrocatalysts. (a) Reproduced with permission from ref. 55. Copyright 2021, American Chemical Society. (b) Reproduced with permission from ref. 56. Copyright 2018, Elsevier. (c and d) Reproduced with permission from ref. 59. Copyright 2022, Elsevier.

which makes it a better catalyst for OER performance, and it may contribute to the OER process by following a similar redox cycle between the Mn^{3+} and Mn^{4+} OER process.[45,53,54]

In order to improve the catalytic activity of β-MnO_2, Gu introduced Ru^{3+} precursor salt in the hydrothermal reaction of β-MnO_2. The crystal splitting phenomenon caused by doping drastically affected the OER and ORR activity of β-MnO_2. After doping, the obtained nanorods exhibit a fragmented structure as shown in Fig. 4a, and the Fourier-transform extended X-ray absorption fine structure (FT-EXAFS) analysis indicates that the Ru-doped sites are mainly interstitial sites within the tunneling structure of β-MnO_2, with some exposure on the surface during crystal splitting, which is the main reason for the elevated OER activity. To explore the active sites for its reaction, DFT confirmed that crystal splitting exposes the atomically dispersed Ru–O species on the MnO_2 surface as OER active sites, while the induced lattice strain and Mn^{3+} state, as well as the abundant oxygen vacancies, can further enhance the ORR activity of the catalyst, which eventually leads to an OER/ORR potential difference of only 0.63 V.[55] Yao *et al.* controlled the concentration of KCl and synthesized β-MnO_2 crystals with a bipyramidal structure with tunable morphology using a simple hydrothermal method (Fig. 4b). *In situ* studies revealed that the K^+ cation influences the morphology of β-MnO_2 crystals by affecting the formation of the α-$K_{0.5}Mn_4O_8$ intermediate phase and the subsequent phase transition process. The elevated concentration of K^+ cations reduced the prism length of β-MnO_2 crystals by affecting the formation of α-$K_{0.5}Mn_4O_8$ nanowires and the tunneling transition process. They speculated that if a suitable surfactant is available to limit the directional attachment of $K_{0.5}Mn_4O_8$ nanowires while maintaining the K^+ cations, it is possible to significantly reduce the size of the β-MnO_2 structure and improve its electrochemical properties. Their work undoubtedly brings current ideas for the design of such materials for applications in supercapacitors, fuel cells, and catalysts.[56]

3.1.3 δ-MnO_2. Birnessite is also expressed as δ-MnO_2 and has a two-dimensional (2D) layered structure. Structurally, the octahedral co-edge element [MnO6] in δ-MnO_2 consists of stable Mn^{4+} and unstable Mn^{3+}. In contrast to the stable Mn^{4+}, the unstable Mn^{3+} is responsible for hydroxide ion adsorption and oxygen evolution; therefore, Mn^{3+} is considered to be the active site in Mn-based oxide catalysis.[57] However, due to the inherently low conductivity and Mn^{3+} concentration, the OER performance of δ-MnO_2 is still lower than that of catalysts based on Fe–Co–Ni benchmarks.

The OER activity of δ-MnO_2 primarily depends on the chemical composition, crystal structure, and morphology.[58] Cheng *et al.* prepared ultra-thin amorphous δ-MnO_2/ε-Fe_2O_3 heterojunction nanosheets with oxygen vacancies, denoted as 0.5Fe–Mn–O (Fig. 4c–d), and the catalyst shows high output OER activity, which requires only 299 and 322 mV overpotential to drive current densities of 100 and 300 mA cm^{-2} and a Tafel slope of only 35.1 mV dec^{-1}. Determination of its indicated chemical state by XPS revealed a higher Mn^{3+} concentration and proportion of defective oxygen in 0.5Fe–Mn–O compared to δ-MnO_2, which was attributed to additional distorted [MnO_6] structural units in δ-MnO_2 caused by evolved intercalated ε-Fe_2O_3. The observations further confirm that 0.5Fe–Mn–O consists of δ-MnO_2/ε-Fe_2O_3 heterojunctions with abundant Jahn–Teller active Mn^{3+}, oxygen vacancies, and Fe^{3+} doping, which facilitates the initiation of interlayer cooperative catalysis and improves OER performance. Further DFT calculations revealed that the oxygen vacancies (Fe–Vo–Mn) immediately adjacent to the Fe and Mn atoms are the optimal OER active sites for the 0.5Fe–Mn–O catalyst, indicating that the oxygen vacancies play an important role in the modified framework for the OER.[59] The two-dimensional LDH(+)–Birnessite(−) hybrid catalyst synthesized by Chen *et al.* exhibited advanced OER catalytic activity and stability with an overpotential of only 407 mV at a current density of 400 mA cm^{-2} and a Tafel of only 43 mV dec^{-1}, indicating that this hybrid catalyst has good potential for electrolysis of water for hydrogen production. The interlayer NiFe LDH (+) also changes the electronic structure of δ-MnO_2 and generates an electric field between NiFe LDH (+) and δ-MnO_2(−), which leads to a significant reduction of the overpotential of the OER. DFT calculations confirm the modulation of NiFe LDH during the OER, and the upward shift of Fe-3d orbitals in LDH promotes the electron transfer from δ-MnO_2 to LDH, which greatly enhances the performance of the OER.[60]

Interlayer cations play an essential role in tuning the electronic structure of δ-MnO_2 materials. An effective method for increasing the catalytic activity of layered manganite oxides was developed by McKendry *et al.* through cooperative doping of a two-dimensional lattice and interlayer. The doping of the MnO_2 lattice with cobalt allows for more efficient hole transport to the active sites of the interlayer iron oxides; meanwhile, the iron hydrazine intercalation procedure reduces the particle size and increases the concentration of Mn^{3+} defects. With the addition of intra-layer cobalt and inter-layer iron, a highly efficient OER catalyst was obtained with an overpotential potential drop of 425 mV compared to birnessite.[61] Pu synthesized efficient catalysts containing nickel in two-dimensional layered metal oxides (δ-MnO_2) by a simple ion-exchange reaction. The intercalation mechanism and oxidation states of nickel and manganese have been explored using the synchrotron X-ray absorption spectroscopy (XAS) technique. It was shown that the intercalation of nickel occurs at the Mn^{3+} site by reducing Mn^{3+} to Mn^{2+} and that the intercalated nickel is the active site for the OER. The synthesis scheme of this work can be broadly applied to provide ideas for the structural development of other layered metal oxides.[62]

In Fig. 4e, we list the overpotentials and Tafel plots of MnO_2 compounded with other materials in recent years, most of which are limited to around 300 mV, and their range of application and catalytic activity is not superior. Although MnO_2 has great potential as a non-precious metal oxide catalyst in the field of water electrolysis, it still suffers from problems such as the small number of active sites. Meanwhile, some researchers have designed different MnO_2 nanomorphologies to increase the number of active sites on the surface, with nanowires exhibiting the highest OER mass activity due to the highest specific surface area and nanotubes exhibiting the highest specific activity due to the high Mn^{3+} surface concentration/surface defects.[63–65] On

the other hand, in addition to the use of monoatomic metals and MnO_2 composites to enhance catalytic activity, Xu *et al.* used MnO_2-NWRS/CNTs, a composite of carbon nanotubes and MnO_2, to show good catalytic activity as well as conductivity in the ORR and OER.[66] We believe that the development of MnO_2 in the field of OER electrocatalysts will be accelerated with the preparation of more advanced materials and the design of chemical compositions based on the existing foundation.

3.2 Mn_2O_3

In the family of MnO_x, Mn_2O_3 has attracted extensive attention in the field of supercapacitors and batteries due to its excellent energy intensity and simple synthesis process. However, there are few types of studies on electrocatalysis.[67,68] The crystal structure of Mn_2O_3 is shown in Fig. 5a, where the Mn^{3+} cation is coordinated to the O anion in an octahedral, orthogonal crystal system.[69] The OER activity of Mn_2O_3 is attributed to the presence of a Jahn–Teller distorted shared edge octahedron occupied by Mn^{3+} (d^4) centers with significantly elongated Mn–O bonds. Due to the asymmetric occupation of e_g orbitals, the bond energy is reduced and the Mn^{3+}–O octahedron is activated to participate in the OER.[70] It has been reported that the overpotential value of Mn_2O_3 is considerably higher than that of other transition metal oxides, and due to the special d-electron structure of Mn_2O_3, it is very difficult to synthesize pure phases of Mn_2O_3.[71] Zhao monitored the OER process on the Mn_2O_3 catalyst surface using *in situ* liquid TEM and observed the development of oxygen nanobubbles around the catalyst in space. In addition, *in situ* TEM observed that the thickness of the amorphous layer on the Mn_2O_3 surface is in a variable state, and they conjectured that the high-valence Mn^{4+} should be reduced to Mn^{3+} in the generation of molecular O_2. This suggests that the amorphous layer on the Mn_2O_3 surface is the

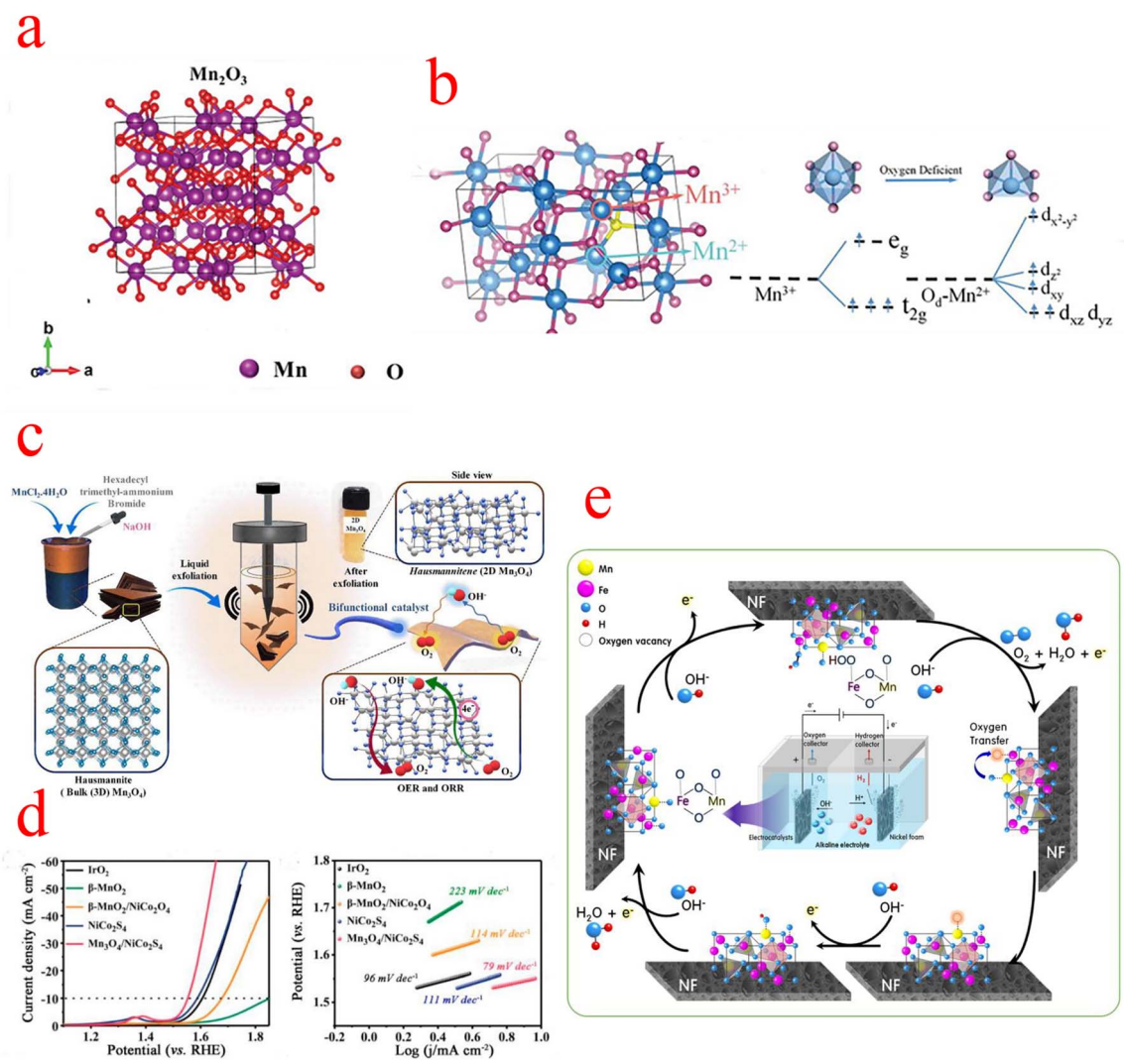

Fig. 5 (a) Mn_2O_3 crystal structure. (b) Crystal structure of Mn_3O_4, octahedra of [MnO_6], and d-orbital splitting conformation. (c) Schematic representation of the liquid phase exfoliation method with Mn_3O_4 formation. (d) LSV curves and Tafel slope plots. (c) The OER process on the $MnFe_2O_4$/NF catalyst. (a) Reproduced with permission from ref. 88. Copyright 2021, John Wiley and Sons. (b) Reproduced with permission from ref. 89. Copyright 2020, John Wiley and Sons. (c) Reproduced with permission from ref. 78. Copyright 2022, Elsevier. (d) Reproduced with permission from ref. 82. Copyright 2020, Elsevier. (e) Reproduced with permission from ref. 87. Copyright 2021, Elsevier.

main active region as well as that the valence of Mn is constantly changing, possibly to be more adapted to the different steps of the OER process.[72] The poor electronic conductivity and relatively low OER dynamics of Mn_2O_3 should be improved by combining with an additional state with higher OER activity. Bigiani used the first row of transition metal (Fe, Co, Ni) oxide nanoparticles (NPs) as OER electrocatalysts in alkaline media. Through plasma-assisted fabrication, Fe_2O_3, Co_3O_4, and NiO NPs can be efficiently dispersed into Mn_2O_3 and form tight oxidation interfacial contacts, which can enhance charge carrier transport and facilitate the diffusion of reactants and products.[73] The unique hollow RuO_2/Mn_2O_3 composite fiber prepared by Yoon shows excellent OER electrocatalytic performance in alkaline media.[74] Another research group, Yang *et al.* synthesized Ni_2P/Mn_2O_3 ultra-high electrochemically active area catalysts by the electrostatic spinning technique, which required only a low overpotential of 280 mV to provide 10 mA cm^{-2} current density, superior to many previously reported Mn_2O_3 catalysts. The large aspect ratio of the one-dimensional nanofibers facilitates electrolyte penetration and oxygen bubble release, and the introduction of Mn modulates the electronic structure of Ni_2P and greatly improves the OER performance.[75]

3.3 Mn_3O_4

Mn_3O_4 belongs to the spinel group, where divalent and trivalent manganese ions are distributed in two distinct lattice sites. The oxygen ions are closely arranged in a cubic form, with divalent manganese ions occupying tetrahedral voids and trivalent manganese ions occupying octahedral voids (Fig. 5b).[76] The general formula of the spinel type is AB_2O_4, which consists of a tetrahedral cation A with a divalent charge and an octahedral cation B with a trivalent charge. The spinel structure is nicely conductive due to the excellent electron transfer between the different oxidation states A^{2+} and B^{3+}.[77] Gowda *et al.* carried out an in-depth study of the origin of the different active sites of the OER and ORR in Mn_3O_4. They synthesized two-dimensional Mn_3O_4 by liquid phase exfoliation (LPE), as shown in Fig. 5c, and DFT calculations confirmed the presence of two sites, Mn(III) and Mn(II), on the (112) oriented surface of Mn_3O_4, which are highly active for the OER and ORR, respectively.[78] In the early studies on Mn_3O_4, electrochemical and spectroscopic techniques were used to characterize their reactivity in the OER.[79] For example, MnO_x films obtained by electrodeposition have a different composition and polycrystalline morphology; after cyclic activation, the $Mn(OH)_2$ generated by the cathode causes a phase transition of (δ-MnO_2) to an intermediate product of (α-Mn_3O_4) type, and the catalytic activity of MnO_x after activation is much higher than that of the original MnO_x. It has been shown that different manganite systems in the literature have different OER activity curves, as different manganite compositions and crystals may be introduced by the preparation methods.[80]

Recently, the synergetic chemical coupling effect and interface structure engineering have played a crucial role in the development of Mn_3O_4 materials. Guo enabled the chemical coupling of active CoO nanoclusters with Mn_3O_4 octahedra; the strong interaction between the two components promotes the formation of a high-energy interface Mn–O–Co and a highly oxidized state of CoO, and this high-energy structure has a large number of active sites that facilitate rapid charge transfer. The starting potential and catalytic kinetic analysis of the catalysts indicate that the OER activity of CoO/Mn_3O_4 is mainly derived from CoO, while the coupling of CoO to Mn_3O_4 further enhances the catalytic performance and provides a higher catalytic activity than the Ru/C OER activity.[81] Mn_3O_4 is the most stable form of MnO_x at high temperatures and can be used as a suitable substrate for the construction of composite structures with other active materials. Wang constructed one-dimensional $Mn_3O_4/NiCo_2S_4$ rod-like nanomaterials based on the two-phase composite of metal oxide and sulfide, and its catalytic activity is shown in Fig. 5d. According to the Kirkendall effect, the outward diffusion of Mn^{4+} and O^{2-} and the sulfidation process of $NiCo_2O_4$ proceed almost simultaneously, which leads to the formation of a considerable number of oxygen defects at the interface of Mn_3O_4 and $NiCo_2S_4$ because the diffusion rate of Mn^{4+} is much faster than the diffusion rate of O^{2-}. The chemical reaction at the interface leads to the formation of vacancies and defects, which can serve as catalytically active sites.[82] Huang's work prepared hybrid catalysts of nanoparticles Co_3O_4/Mn_3O_4 anchored on (reduced graphene oxide) rGO substrates. Although Co_3O_4 has excellent ORR/OER activity, it is very unstable at high current densities, and the introduction of Mn_3O_4 exactly addresses this issue. Meanwhile, the large specific surface area provided by the layered rGO facilitates the contact between the catalyst and the electrolyte, thus improving the utilization of active sites and the reaction kinetics. In addition, DFT calculations showed that after coupling Mn_3O_4 (211) with Co_3O_4(111), the $\Delta G_{MOH\rightarrow OH}$ value on the Mn_3O_4 (211) surface of Co_3O_4/Mn_3O_4 was close to -1.23 eV, which is the conceptual value of $\Delta G_{MOH\rightarrow OH}$ for the catalyst at 0.4 V equilibrium potential at pH = 14, yielding that the Co_3O_4/Mn_3O_4 Mn_3O_4 (211) surface is the active surface for the ORR/OER.[83] Cho and his team demonstrated a breakthrough synthesis of 4 nm Mn_3O_4 nanoparticle (NPs) catalysts with an overpotential of only 395 mV at 10 mA cm^{-2}, a performance superior to any other Mn-, Fe-, Co-, and Ni-based electrocatalysts reported so far under neutral conditions. They then further optimized their catalytic performance by Ni doping, and XRD analysis showed Ni doping-induced lattice distortion of the Mn_3O_4 NPs, which also led to the production of distorted octahedral Mn(III) species, enhancing the number of active sites in the OER. According to electrokinetic studies, the OER catalytic mechanism of pristine and 5% Ni-doped Mn_3O_4 NPs is similar, namely involving reversible one-electron and one-PCET processes prior to the RDS. This implies that the doping of Ni in Mn_3O_4 NPs does not affect the OER mechanism under neutral conditions. The enhanced activity of Ni doping may be due to the promotion of this step of O–O bond formation.[84–86]

Some research groups use low-cost transition metal spinel materials as OER catalysts. Kim synthesized Mn–Fe-based materials with a spinel structure and proposed the OER mechanism on the $MnFe_2O_4$/NF electrode during water electrolysis in an alkaline solution (Fig. 5e). The OH^- ions decomposed in

water combined with the lattice oxygen of Fe^{2+} and the FeO in $MnFe_2O_4$ is oxidized to Fe–OOH (Fe^{3+}). In the next step, Fe–OOH continues to be converted to Fe–OO by OH^-, and then O_2 is oxidized and desorbed. After O_2 is generated, oxygen vacancies are formed in the iron lattice of the anode catalyst. At this point, Mn^{3+} with strong reducing power moves the oxygen in its lattice through the spinel lattice into the vacancies generated around Fe^{2+}, which is then reduced to Mn^{2+}. After that, the oxygen vacancies formed in the Mn^{2+} lattice are rapidly filled with OH^- ions in water and regenerated into Mn^{3+} ions. Through this process, the $MnFe_2O_4$ spinel lattice is restored to its initial state. In conclusion, the synergistic oxygen transfer process between Fe^{2+} (or Fe^{3+}) and Mn^{3+} (or Mn^{2+}) catalytic species in the $MnFe_2O_4$/NF of the OER anode contributes to the long-term stability of the catalytic electrode for the OER.[87]

4. MnO_x issues and strategies

MnO_x is a potential OER catalyst whose oxides exist in more than 30 different stable polycrystalline forms, and the crystal structure and variable valence states are key to improving its electrostatic properties.[44,90,91] However, their electrocatalytic activity is still not sufficient to replace noble metal oxides. To explore efficient MnO_x electrocatalysts, it is essential to clarify the dominant factors controlling the electrocatalytic activity of these oxides.[92] Above we have comprehensively reviewed the progress of MnO_2, Mn_3O_4, and Mn_2O_3 materials, many of which have encountered several common problems such as Jahn–Teller distortion, active sites, stability, *etc.* These critical issues have hindered the understanding of catalytic reaction mechanisms and the development of efficient and stable catalysts.

4.1 Jahn–Teller distortion

Jahn–Teller distortion is very common in Mn-based materials, and it is believed that the presence of Mn^{3+} can induce this phenomenon, thereby explaining the structural degradation of Mn-based electrode materials.[93] The high spin electron configuration of the Mn(III) $(t_{2g})^3(e_g)^1$ octahedron in the octahedral unit usually experiences Jahn–Teller distortion, resulting in long and flexible Mn–O bonds, for the OER, $(e_g)^1$ is considered to be the best electronic configuration for transition metal-based catalysts.[94] Compared with manganese(IV), the d^4 electron configuration of manganese(III) is more inclined to show the Jahn–Teller effect. In addition, based on the strong Jahn–Teller effect, the transition from Mn^{4+} to Mn^{3+} inevitably prolongs the Mn–O bond and causes electron redistribution on the surface.[95,96]

Kang *et al.* stabilized the Jahn–Teller active Mn^{3+} species by replacing the Mn^{4+} ions with the more electronegative Ru^{4+} ions (Fig. 6a), which led to the stabilization of the Jahn–Teller active Mn^{3+} species and also provided the electronegative Ru sites. Due to bond competition, the adjacent (Mn–O) bond is weakened by (Ru–O), leading to distorted $[MnO_6]$ octahedra with elongated (Mn–O) bond distances, which stabilizes the Mn^{3+} ion. Although Ru substitution also provides electrocatalytically active Ru sites for α-MnO_2, this contribution is smaller than the stabilization of Mn^{3+} species caused by adjusting the (Mn–O) bond covalency.[97] Yang proposed a strategy to thermally induce structural deformation of calcium manganese ore ($CaMnO_3$, denoted as CMO) to improve the oxygen catalytic activity of CMO. When O atoms were partially extracted from CMO (denoted as D-CMO), the structure of $[MnO_6]$ octahedra was deformed due to the Jahn–Teller effect (Fig. 6b). They used simulations to model the reaction pathway of the OER (Fig. 6c). The Mn cation on the surface can coordinate with OH^- to form an Mn–OH bond, O–Mn–O(OH) is the starting point of the OER process, while the third step with the formation of OOH* ($O^* + OH^- \rightarrow OOH^* + e$) is the rate-determining step (RDS), and the RDS shows that the theoretical overpotential of the OER for D-CMO (0.74 V) is lower than that of CMO (0.82 V). When O_2 is adsorbed on D-CMO, the average number of electron transfers from Mn to O atoms is more than that of CMO. This means that the Mn–O and strong interactions are shorter, which contributes to the activation of O_2 and reduces the Gibbs free energy of the activation step ($* + O_2 \rightarrow O_2*$).[98] The above examples demonstrate that the strategy of inducing $[MnO_6]$ octahedral deformation using the Jahn–Teller effect can provide a new and effective way to improve the electrocatalytic properties of MnO_x.

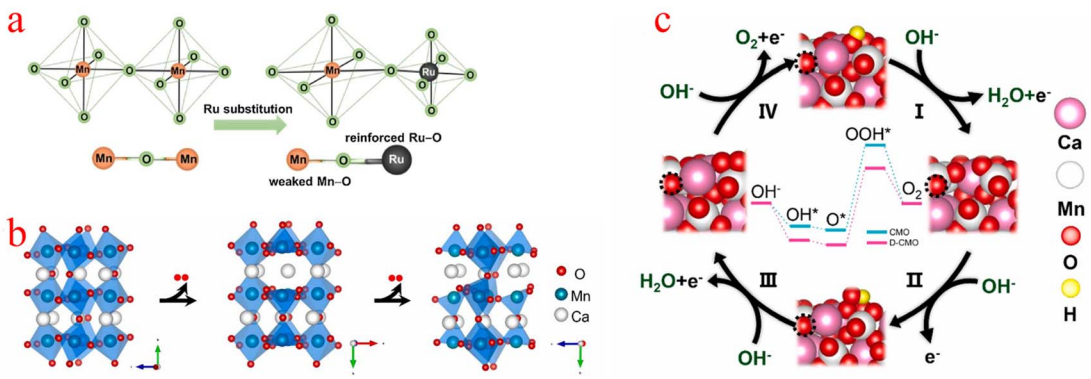

Fig. 6 (a) Schematic diagram of the evolution of the adjacent (Mn–O) bond when the (Ru^{4+}–O) bond is incorporated into the α-MnO_2 lattice. (b) Schematic diagram of the crystal structure process of O in $CaMnO_3$ being extracted. (c) Reaction pathways and corresponding reaction free energy diagrams for the OER of CMO(121) and D-CMO(121) at 1.23 V potential. (a) Reproduced with permission from ref. 97. Copyright 2018, Elsevier. (b and c) Reproduced with permission from ref. 98. Copyright 2021, Elsevier.

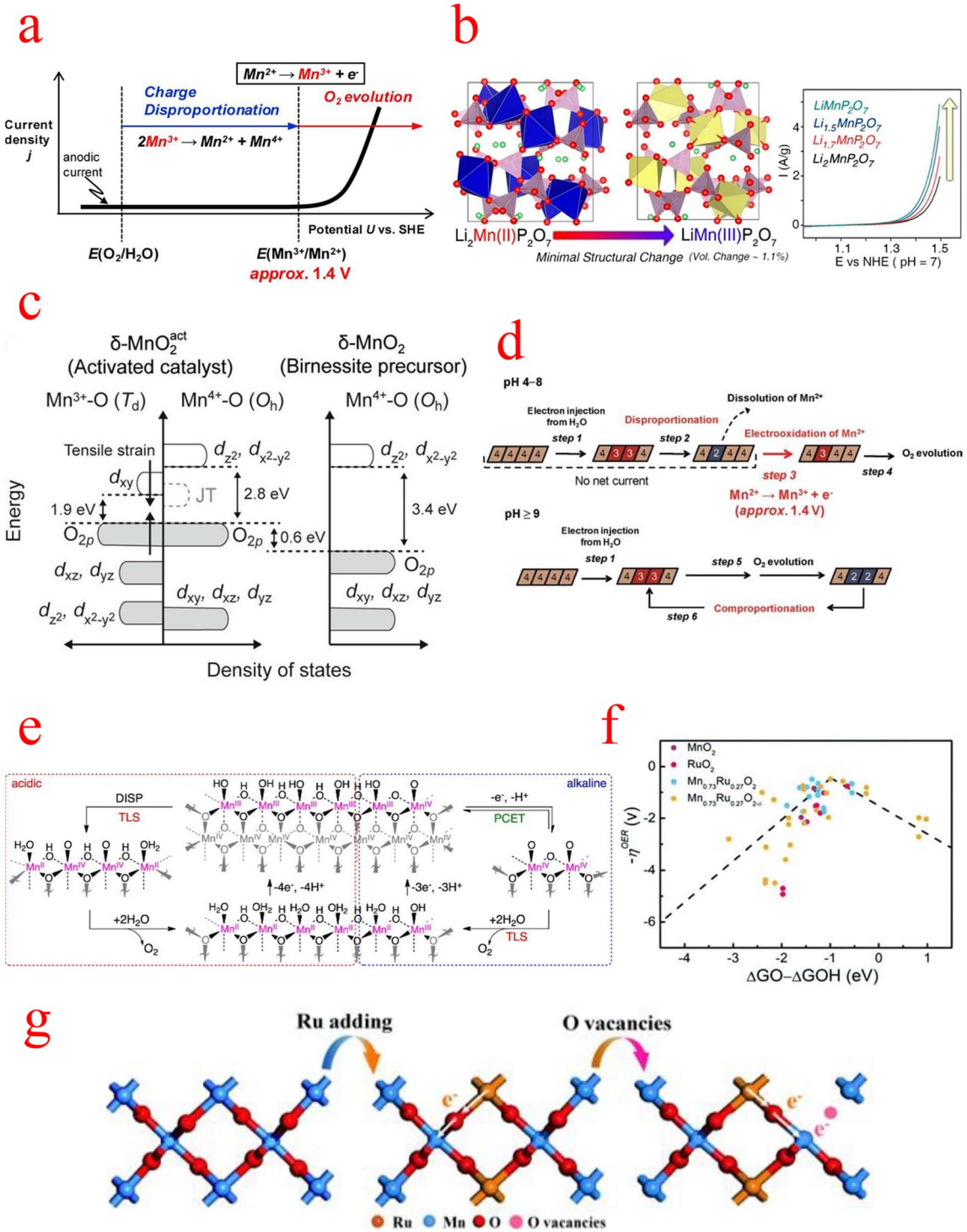

Fig. 7 (a) Schematic illustration of a current density (j) *vs.* potential (U) curve for a pristine δ-MnO_2 electrode under neutral pH conditions. (b) Increase in the average oxidation state of Mn from 2 to 3 in $Li_{2-x}MnP_2O_7$ and schematic representation of the catalytic performance. (c) Schematic diagram of the band structure of the activated catalyst system derived from the "α-Mn_3O_4-3e" model. (d) Schematic diagram of the oxidation state of Mn ions in the δ-MnO_2 reaction at different pH values. (e) Proposed mechanism for the OER on MnO_x under (left) acidic and (right) alkaline pH conditions. (f) Schematic free energy profiles of overpotential results *versus* the difference between the adsorption energies of O* and OH* intermediates for MnO_2, *etc.* in acid media. (g) A schematic diagram of the charge redistribution process in $Mn_{0.73}Ru_{0.27}O_{2-\delta}$. (a) Reproduced with permission from ref. 101. Copyright 2012, American Chemical Society. (b) Reproduced with permission from ref. 102. Copyright 2014, American Chemical Society. (c) Reproduced with permission from ref. 105. Copyright 2018, Proceedings of the National Academy of Sciences of the United States of America. (d) Reproduced with permission from ref. 107. Copyright 2012, American Chemical Society. (e) Reproduced with permission from ref. 108. Copyright 2014, American Chemical Society. (f and g) Reproduced with permission from ref. 109. Copyright 2022, RSC Publishing.

4.2 Active sites

The second is the question of active sites in MnO_x. A remarkable correlation between the amount of Mn^{3+} and the catalytic activity of the OER has been reported. Therefore, strategies to increase the activity of MnO_x must take into account the enhancement and stabilization of the Mn^{3+} species amount. Numerous previous studies have also improved the catalytic performance by introducing Mn(III) in different crystalline phases and found that a large amount of Mn(II) and Mn(III) was oxidized to Mn(IV) in electrocatalytic tests, leading to a decrease in activity.[99,100]

Back in 2012, Takashima's group found that the low catalytic activity of MnO_2 under neutral conditions can be attributed to the instability of Mn^{3+}, whose accumulation on the catalytic surface requires Mn^{2+} oxidation at a potential above 1.4 V, as shown in Fig. 7a. They effectively stabilized the Mn^{3+} species by the formation of N–Mn bonds through the coordination of amine groups with the Mn sites on the MnO_2 electrode surface, and *in situ* spectroelectrochemical techniques demonstrated that stabilization of surface-associated intermediate Mn^{3+} species is an effective strategy to reduce the electrolytic water overpotential of MnO_2.[101] Later, Park, *et al.* in 2014 chose a pyrophosphate-based Mn compound ($Li_2MnP_2O_7$) as a model system and observed the effect of the Mn(III) state itself on water oxidation catalysis by adjusting the manganese valence in Li_2-MnP_2O_7. Remarkably, the OER catalytic performance increases continuously as the average oxidation state of manganese in $Li_{2-x}MnP_2O_7$ increases from 2 to 3, as shown in Fig. 7b.[102]

In recent years, more scholarly studies have pointed out that Mn^{3+} is the active center of the OER, and its electronic configuration is $(t_{2g})^3(e_g)^1$, which plays an important role in the water oxidation reaction because the e_g orbital is involved in the σ-bonding to the anion adsorbate, the occupancy of this orbital directly determines the binding energy of the reactants and leads to a volcano-like activity profile.[94] Higher Mn^{3+} content in the manganese group is beneficial for enhancing the adsorption of –OH at the catalyst surface, and higher surface oxidation valence states are also beneficial for improving the OER activity of manganese-based materials.[103] In studying the OER activity of β-MnO_2 on the (101) and (110) faces, Nakamura's group found that the interlayer charge ratios of Mn^{2+} and Mn^{4+} produced two Mn^{3+} species on the (101) face, resulting in 11 times more Mn^{3+} coverage on the (101) face than on the (110) face, and thus a higher OER activity on the (101) face.[104] The study by Chan *et al.* explained that the presence of Mn^{3+} enhances the catalytic effect of the OER. They observed through Raman spectroscopy that the Mn^{3+} tetrahedron (T_d) produces local strain on the oxide lattice. This strain causes the O 2p valence band to be higher than the Mn^{3+} tetrahedron (T_d) and Mn^{4+} octahedron (O_h) valence bands and leads to the gap between the highest occupied molecular orbital (HOMO) and the lowest unoccupied molecular orbital (LUMO) to decrease, while the reduced HOMO–LUMO gap promotes the oxygen evolution reaction. As shown in Fig. 7c, the Mn^{3+} ions at the Td site are unable to form Mn^{4+}, which causes a rearrangement of the Mn-d and O 2p states and promotes the formation of oxygen vacancies, factors that facilitate the OER to produce oxygen.[105] Moreover, in the study of spinel structures, the nature of their OER activity is also closely related to the valence states of Mn. Wei found that Mn in the octahedral sites was identified as the active site of $MnCo_2O_4$ and that the ORR/OER activity of $MnCo_2O_4$ exhibited a volcanic shape as a function of the Mn valence state in the octahedra, while the apex of the ORR/OER volcanic trend was located at the position of the Mn valence state ≈ +3.[106]

4.3 Stability of MnO_x

Experimental and theoretical work on MnO_x catalysts has emphasized the role of Mn(III) as an essential intermediate state for achieving catalytic reactions. Regardless of the initial Mn oxidation state in the catalyst, Mn(III) is generated and participates in the water oxidation process. Therefore, the question of the stability and reconstruction of Mn^{3+} in MnO_x needs to be discussed next.[102]

MnO_x can act as an effective electrocatalyst under strongly alkaline conditions but is inefficient under neutral and acidic conditions. In a 2012 review, Takashima *et al.* investigated the OER process in MnO_2 and found fundamentally different mechanisms for the OER in acidic, neutral, and basic conditions. At pH < 9, the larger overpotential is due to the rapid consumption of Mn^{3+} by the disproportionation reaction, as shown by the following reaction:

$$2Mn^{3+}(aq) + 2H_2O \rightarrow MnO_2(s) + Mn^{2+}(aq) + 4H^+$$

while at pH ≥ 9, the disproportionation of Mn^{3+} is effectively inhibited, which leads to a very easy accumulation of Mn^{3+} in the MnO_2 layer, resulting in a large decrease in the overpotential; moreover, in this pH region, the comproportionation reaction between Mn^{2+} and Mn^{4+} contributes to the regeneration process of Mn^{3+} (Fig. 7d). Therefore, the pH of the electrolyte has a significant effect on the productivity and accumulation of Mn^{3+}, which further affects the electrocatalytic performance.[107] Subsequently, Huynh *et al.* performed a kinetic study of the OER mechanism of MnO_x over a range of pH values under acidic, neutral, and alkaline conditions. Tafel and reaction order analyses reflect two competing mechanisms: a single-electron single-proton PCET pathway, which dominates under alkaline conditions, and an Mn^{3+} disproportionation process, which dominates under acidic conditions (Fig. 7e). Another significant point of this study is that it shows that MnO_x has a high intrinsic and functional kinetic stability in acidic electrolytes and its ability to remain self-healing for electrolytes with a pH greater than zero, and MnO_x can undergo the OER in extremely acidic environments.[108] As for the development of MnO_x in acidic media, Wang's group has made new progress. They developed Mn–Ru solid-solution oxides with oxygen vacancies (named $Mn_{1-x}Ru_xO_{2-\delta}$), which is currently the better-performing MnO_x catalyst in acidic electrolytes. Among the synthesized catalysts, $Mn_{0.73}Ru_{0.27}O_{2-\delta}$ with the optimized electronic structure only requires an overpotential of 208 mV to produce a current density of 10 mA cm^{-2} in an acidic electrolyte and a Tafel slope of 65.3 mV dec^{-1}, which exceeds RuO_2 and

most noble metal-based OER electrocatalysts. The volcano diagram and the difference between the overpotential results and the adsorption energies of the O* and OH* intermediates are shown in Fig. 7f. The $Mn_{0.73}Ru_{0.27}O_{2-\delta}$ model is at the peak of the volcano diagram, indicating the lowest overpotential value for the OER of all models studied. DFT calculations show that the introduction of Mn can alter the RDS transition from O* → OOH* to OOH* → OO*. In addition, EXANES shows that the valence of the Mn species increases significantly after the OER process, while the valence of the Ru species remains almost unchanged, indicating that the Mn atom is converted into an electron donor and that the Ru species is the true OER active site (Fig. 7g).[109]

Normally speaking, the $(t_{2g})^3(e_g)^1$ orbital and exceptionally stable Mn^{3+} ions in MnO_x are extremely vital to improving their catalytic performance; on the other side, more and more studies have been carried out on the octahedral unit of $[MnO_6]$ because the structural changes caused by octahedral distortion can strengthen the orbital interaction between the Mn center and oxygen intermediate, thus considerably promoting the oxygen catalytic kinetics. Therefore, to design high-catalytic activity manganese-based catalysts, it is necessary to consider factors such as the active sites of the electronic orbitals. In the following part of this chapter, we propose some improvements for reference, such as defect engineering (introducing vacancies), interface engineering (heterogeneous interfaces), *etc.*

4.4 Improvement strategies

4.4.1 Defects caused by vacancies. As a means to further improve the electronic properties of two-dimensional materials, researchers are increasingly concerned about the relationship between defect engineering (vacancy) and structure performance. Previous studies have shown that appropriate vacancies can alter the physical properties (Fermi energy levels, electrical conductivity, *etc.*) and adsorption properties of materials. Therefore, the introduction of vacancy defects is an effective strategy to improve the catalytic performance of MnO_x.[110–113] Lu adjusted the electronic structure of MnO_2 by inserting transition metal cations and increased the content of Mn^{3+} and oxygen vacancies (Fig. 8a). With the insertion of Fe, Co, and Ni cations into the MnO_2 layer, the Mn ions of MnO_2 transform from the stable d^3 (Mn^{4+}) state to the unstable deeply rotated d^4 state (Mn^{3+}) generating extra oxygen vacancies in the MnO_2 structure according to the equation.

$$-Mn^{4+}-O_2-Mn^{4+}- \rightarrow -Mn^{3+}-*-Mn^{3+}-+1/2O_2$$

where * represents the formation of oxygen vacancies. It was further shown by XPS that the cation-embedded MnO_2/NF material has a higher concentration of oxygen vacancies than before, thus improving the ability of the material to adsorb free OH^- when performing catalytic reactions. The group also concluded that the synergistic effect of oxygen vacancies and Mn^{3+} ions after the introduction of cations was the main reason for the superior catalyst performance, with the modulation effect being more pronounced than that of Co^{2+} and Ni^{2+} due to the higher oxidation valence of Fe^{3+}, which generates more Mn^{3+} sites. [103] Zhao grew two monolayer-thick δ-MnO_2 nanosheets on nickel foam using the *in situ* growth method, and the OER properties can be attributed to the ultrathin δ-MnO_2 nanosheets containing a large number of oxygen vacancies, which promote the formation of Mn^{3+} active sites, resulting in semiconducting properties and strong H_2O adsorption capacity.[114] Liu *et al.* introduced anionic oxygen and cationic manganese vacancies (VO and VMn) into MnO_2 nanosheets. To elucidate the synergistic effect of VMn and VO on improving HER/OER kinetics, the calculation of electrochemically active surface area (ECSA) shows that oxygen vacancies enhance the active site, while the impedance indicates that VMn production is beneficial for improving conductivity. The possible HER and OER mechanisms are depicted in Fig. 8b. Under alkaline conditions, water molecules are adsorbed on the bridge site of two adjacent Mn atoms located in the DV (double vacancy), which then splits with the help of nearby O to produce H_2 and free OH^-. Similar to the OER, the dissociated OH^- is adsorbed on the same bridge sites to form the Mn–O(H)–Mn intermediate. Subsequently, Mn–O(H)–Mn combines with OH^- to release water molecules, which then become Mn–O–Mn. The metastable Mn–O–Mn intermediate will combine with OH^- to produce Mn–OOH and eventually release O_2. DV-MnO_2 exhibited excellent catalytic performance with the assistance of synergistic double vacancies, with HER and OER overpotentials of 59 mV and 260 mV, respectively, and Tafel slopes of 63 mV dec^{-1} and 40 mV dec^{-1}.[115] These studies suggest that oxygen vacancies can modulate the catalyst energy band structure and act as active sites for the OER, while the introduction of cations mainly modulates the active center and increases the content of Mn^{3+} and oxygen vacancies. In addition to these strategies for cations and oxygen vacancies, the introduction of additional anions (*e.g.* S) can control the electronic spin state of transition metals and thus increase their OER/ORR catalytic activity,[116] although such studies are not common in MnO_x, which we consider to be an equally effective strategy.

4.4.2 Interfacial heterostructure. Engineering of interfaces is considered one of the most promising strategies for the development of efficient electrocatalysts. The construction of atomically heterogeneous interfaces can effectively tune the electronic and band structure of the catalysts to provide appropriate adsorption/desorption behaviors that improve the electrocatalytic performance.[117–119]

Ni_xS_y@MnO_xH_y/NF constructed by Wang exhibits excellent activity and stability in alkaline solutions. Since the Ni_xS_y electrocatalyst is easily oxidized to the corresponding metal oxides/(oxygen) hydroxyl oxides during the OER, the MnO_x shell protection strategy can effectively improve its catalyst stability. The integration of MnO_xH_y and Ni_xS_y forms a heterostructure with abundant Mn–S bonds(Fig. 8c), leading to stronger electronic interactions, and its activity may be the conversion of NiS into amorphous Ni species (NiO_xH_y), while the synergistic interaction between MnO_xH_y and Ni_xS_y significantly accelerates the kinetics of HER and OER processes and enhances the charge transfer, and the OER performance remains intact after 5000 CV cycles (Fig. 8d).[120] Niu *et al.* constructed nanowire porous structures using low nitrogen acetic acid (NTA) as

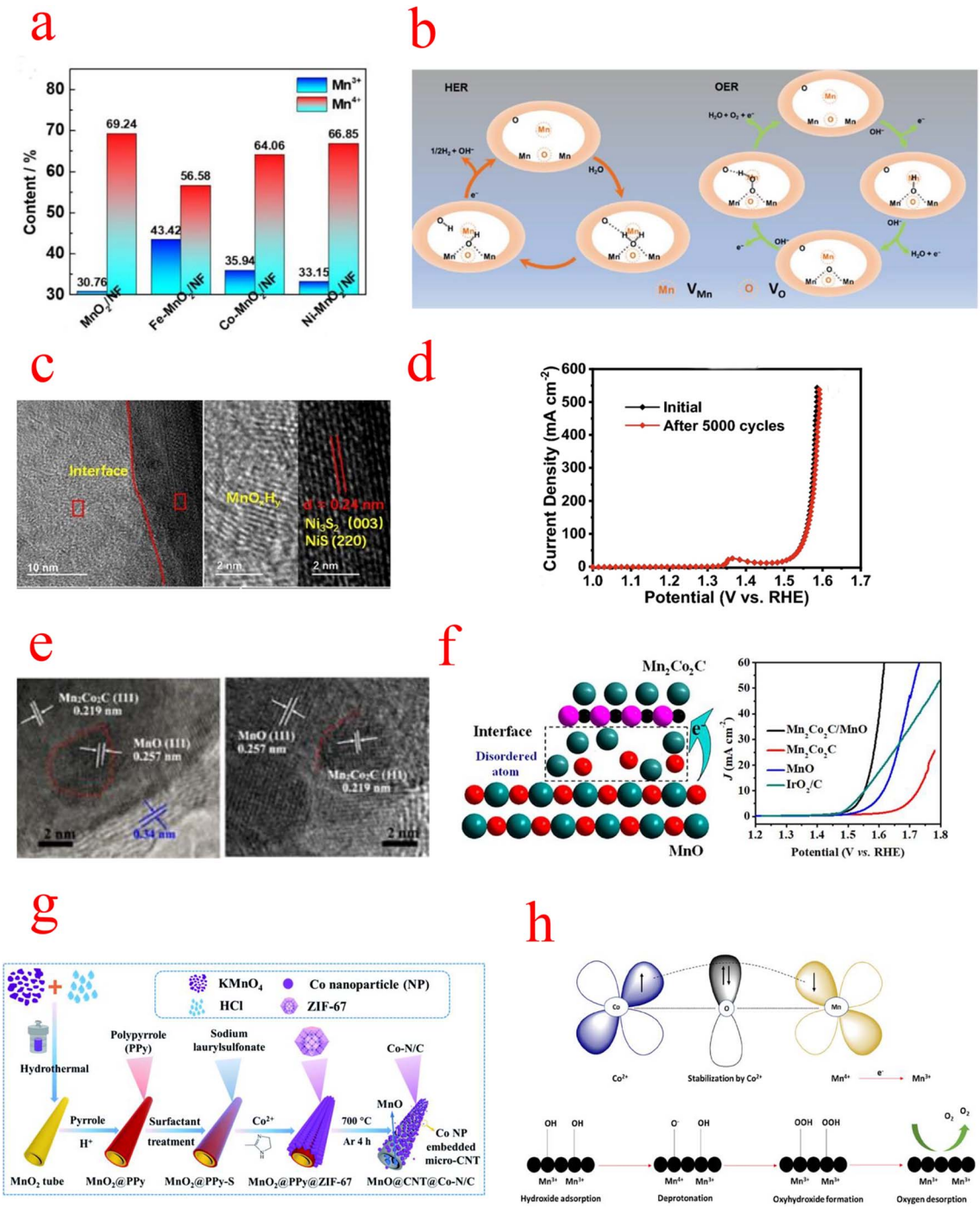

Fig. 8 (a) Schematic illustration of the formation of Fe–MnO_2/NF. (b) Schematic illustration of the HER and OER processes of DV–MnO_2 under alkaline conditions. (c) HRTEM images of Ni_xS_y@MnO_xH_y nanorods. (d) Comparison of LSV curves for Ni_xS_y@MnO_xH_y before and after the 5000-cycle stability test. (e) HRTEM images (f) schematic catalytic mechanism of Mn_2Co_2C/MnO. (g) Schematic illustrating the preparation of the 1D MnO@CNT@Co–N/C hierarchical nanostructure. (h) Probable OER mechanistic pathway (a) Reproduced with permission from ref. 103. Copyright 2021, Elsevier. (b) Reproduced with permission from ref. 115. Copyright 2021, John Wiley and Sons. (c and d) Reproduced with permission from ref. 120. Copyright 2022, Springer Nature. (e and f) Reproduced with permission from ref. 122. Copyright 2020, American Chemical Society. (g) Reproduced with permission from ref. 123. Copyright 2021, Royal Society of Chemistry. (h) Reproduced with permission from ref. 124. Copyright 2022, American Chemical Society.

a chelating agent to stabilize Mn^{2+} and Co^{2+} metal ions. MnO_x alone is not effective as a bifunctional catalyst due to its insufficient OER activity and electron transfer rate limitation, so the synergistic effect between the metal Co and MnO_X was exploited to design bifunctional electrophiles for OER and ORR catalysts. In particular, a strong charge exchange between Co

Table 1 Summary of preparation methods and OER properties of MnO_x composites[a]

MnO_x composite catalysts	Overpotential (mV)	Tafel slope (mV dec^{-1})	Catalyst morphology/support template/catalyst loading	Synthetic method	Ref.
CoO/MnO	280	67.9	Porous nanowires and nanosheets/NF/—	Hydrothermal and vacuum annealing	139
CoP/MnO	230	95	One-dimensional hollow nanofibers/carbon paper/2 mg cm^{-2}	Electrospinning technology, thermal annealing, and phosphating process	140
CoFe@CNT/MnO	193	82	Nanoparticles/CFP/—	Hydrothermal and CVD pyrolysis	141
MnO_x/NiFe-LDH	174	48	Nanosheets/FTO/—	Atomic layer deposition (ALD) and hydrothermal	142
MnO_x/NiFe-LDH/NF	265	73	Nanosheets/NF/—	Hydrothermal and electrodeposition	143
Fe_3O_4@MnO_x	188	77.6	Hierarchical flower-like core–shell microsphere/NF/—	Hydrothermal	144
MnO_x/NiFeP/NF	247	59.8	Nanosheets/NF/—	Hydrothermal phosphating and electrodeposition	145
MnO/Co-CNTs	420	59	1-D hollow tube and particles/glassy carbon/—	High-temperature sintering and growth on carbon nanotubes	146
MnO/Co/PGC	300	77	Nanoparticles/rotating disk electrode RDE/—	Hydrothermal and high-temperature calcination	147
Co/MnO/NC	379	101	Nanometric grain size/GCE/30 μg cm^{-2}	Solvothermal and calcination annealing	148
Mn_2Co_2C/MnO	320	80	Nanocubes and nanoparticles/glassy carbon electrode/—	Coprecipitation and pyrolysis	122
Co/MnO@NC	235	53	Nanowire and nanoparticles/—	Solvothermal and pyrolysis	121
Mn_3O_4@CS/CP	290	95	Spheres/glassy carbon/204 μg cm^{-2}	Hydrothermal and high-temperature calcination	149
Mn_3O_4/CoP	306	51.8	Nanorod and nanoparticles/NF/1 mg cm^{-2}	Hydrothermal	150
$MnFe_2O_4$/NF	310	65	Particles/NF/40 mg cm^{-2}	Hydrothermal	151
Mn_3O_4/$NiCo_2S_4$	320	79	1D rod-like structure and sheet-like/glassy carbon/0.38 mg cm^{-2}	Hydrothermal and annealing	152
Co_3O_4/Mn_3O_4	360	78.2	Nanoparticles/carbon paper/0.382 mg cm^{-2}	Hydrothermal	153
RuO_2/$(Co, Mn)_3O_4$	270	77	Nanoparticles/commercial carbon cloth/—	Hydrothermal	154
N–C/Mn_2O_3	347	75.5	Star-like structure with rough surface/NF/—	Hydrothermal and annealing	155
MnO/CoMn alloy@N	300	—	Nanoparticles/glassy carbon/0.28 mg cm^{-2}	Annealing	156
Co/MnO@N–C	350	84.5	The loosened foam-like/glassy carbon/0.6 mg cm^{-2}	Hydrothermal and pyrolysis	157
MnO/Co@NGC	326	90	Cubical/glassy carbon/—	Pyrolysis	158

[a] CFP: carbon fiber paper; FTO: fuorine-doped tin oxide; NF: nickel foam; GCE: glassy carbon electrode; RDE: rotating disk electrode.

(200) and MnO_X (200) occurs at the heterogeneous interface between metal Co and MnO_X. This means that the O atoms can easily gain electrons from the Co atoms, which leads to a change in the electronic structure of pristine manganites, and charge redistribution facilitates the formation of abundant catalytically active sites on the OER and ORR surfaces.[121] Meng prepared Mn_2Co_2C/MnO catalysts with cubic porous structures by pyrolysis, and TEM revealed the presence of abundant heterogeneous interfaces between Mn_2Co_2C and MnO (Fig. 8e), while XPS confirmed that MnO has an elevated oxidation state [$Mn^{(2+\delta)+}$], which is favorable for OH^- adsorption and subsequent desorption processes. In addition, extended EXAFS measurements further revealed the presence of disordered Mn/O atoms and dangling bonds at the heterogeneous interfaces, which act as additional active sites for adsorption/desorption (Fig. 8f).[122] Interfacial engineering is not a combination of any two catalysts. As mentioned above, there are interfaces that increase the conductivity of a single component, others that increase the active site, and a combination that achieves small reaction activation energies by modulating the energy band structure. Shell–core interfaces have also been designed to take advantage of the durability of MnO_x. However, the active sites of MnO_x heterojunctions are mostly catalysts of another set of components, and how to design catalysts with MnO_x as the active center is a future trend.

4.4.3 Combination with MOFs. Metal–organic frameworks (MOFs) consist of coordination bonds between metal ions and various organic linkages, displaying tunable pore size and composition, extremely ordered porous crystal structures, and high surface areas.[125,126] These characteristics make MOFs promising for applications in catalysis, energy storage, and conversion.[127–129]

MnO_x can be used not only as a framework for metal–organic structures but also as a catalyst for the ORR/OER, which is commonly combined with conductive materials (conductive polymers or carbon materials) to enhance their electrical conductivity and catalytic properties. Li grew polypyrrole (PPy) nanotubes (NTs) and zeolite imidazole framework-67 (ZIF-67) sequentially on MnO_2 NTs as the substrate and oxidant, and subsequently formed a one-dimensional (1D) layered ternary nanocomposite by sintering, as shown in the flow chart in Fig. 8g. The MnO_x particles separated in carbon nanotubes (CNTs) have a mixed valence of $Mn^{2+/4+}$, which can greatly facilitate the diffusion of electrolytes and electron transfer in redox reactions. In addition, the Co–N/C formed on CNTs provides multiple catalytically active sites (*e.g.*, Co–N_x, Co–O, and C–N molecules), and the MnO@CNT@Co–N/C catalysts exhibit better activity and durability compared with commercial catalysts of noble metals.[123,130] Wang introduced Mn species into the zeolite-imidazole frameworks (ZIFs) and then further pyrolyzed the Mn-containing bimetallic ZIFs to synthesize Co@Co_4N and MnO embedded in porous N-doped carbon nanocubes. The introduction of Mn species not only increased the surface content of pyridine/graphitized N and Co_4N in Co@Co_4N/MnO-NC but also converted during calcination to the MnO phase. These high pyridine/graphitic N and moderate MnO species provide efficient catalytic performance for the ORR, while the uniformly distributed Co@Co_4N nanoparticles ensure an abundance of active sites for the OER.[131,132] Selvasundarasekar *et al.* constructed a bimetallic ZIF catalyst containing Co and Mn metal ions and formed the fibers by the electrospinning technique. Molecular orbital studies evaluated the active centers of the bimetals and found that the Co^{2+} concentration inhibits the Jahn–Teller distortion produced by Mn^{3+}, while OER activity is mainly attributed to Mn^{3+} ions and a moderate amount of Co^{2+} leads to a stronger overlap between the anti-bound Mn^{3+} e_g orbitals and oxygen adsorbed O 2p orbitals, enhancing the shorter binding nature of the OER intermediates on the catalytic surface. And a detailed OER mechanistic pathway was hypothesized (Fig. 8h). First, Co^{2+} is initially stabilized by the high oxidation of Mn(IV), then it is reduced to Mn^{3+}, after which OH^- ions are adsorbed on the Mn^{3+} catalytic surface and subsequently it is converted to oxides and oxyhydroxides. Finally, O_2 is desorbed from the catalytic surface. The work of these individuals provides ideas for the search for active centers in bimetallic site catalysts.[124]

4.4.4 MnO_x composites. Finally, we show some other MnO_x composites in Table 1, such as MnO_x/carbon composites, MnO_x/metal oxide composites, and MnO_x/phosphide composites. The Fe_3O_4/MnO_x, CoP/MnO, and MnO_x/NiFe-LDH composites in Table 1 show good electrocatalytic activity. In this case, the molar ratio of the manganese to oxygen atoms deviates significantly from the stoichiometric ratio of the composition, where the manganese ions have mixed valence. In addition, Mn^{4+} and Mn^{3+} species enriched in MnO_x also act as active catalytic centers, which can greatly accelerate electrocatalytic activity.[133–135] On the other hand, this is attributed to chemical coupling and synergistic effects between metal oxides. It is also possible that the smaller volume of the manganite may also provide additional active sites and accelerate the generation of cavity charge carriers.[136–138] These unique properties confer exceptional electrocatalytic properties to the MnO_x composites.

5. Summary and perspectives

This feature article first explains the conventional adsorption mechanism of the OER in alkaline environments, then presents the progress of different MnO_x studies on the OER, and presents the catalytic mechanism of MnO_x with several strategies for improvement. As far as the current study is concerned, MnO_x as an anode catalyst can reduce the OER excess potential and is an electrocatalyst that could be developed for the electrolysis of water. For MnO_2, the catalytic activity depends primarily on the crystal structure, morphology, size, pore structure, and surface oxidation state of the manganese atoms. It has been found that the catalytic activity of α-MnO_2 in the OER is higher than that of β-MnO_2 and δ-MnO_2 in early research. More importantly, the large interlayer spacing of MnO_2 allows for the insertion of additional ions, which affects its catalytic performance. Next, for Mn_2O_3, the presence of distorted octahedra occupied by the $Mn^{3+}(d^4)$ center elongates the Mn–O bond due to the Jahn–Teller effect in Mn_2O_3, and the Mn^{3+}–O octahedra are activated to participate in the OER. Due to its special d-electron structure,

Mn_2O_3 has a much higher overpotential than other transition metal oxides. In this respect, the poor electronic conductivity and relatively low OER dynamics of Mn_2O_3 are mostly improved by combining them with other catalysts with higher OER activity. Mn_3O_4 with a spinel structure has tetrahedral and octahedral centers occupied by $Mn^{3+}$and Mn^{2+} ions, respectively, and it has been demonstrated that Mn^{3+} and Mn^{2+} in Mn_3O_4 affect its OER and ORR performance. In addition, the spinel oxide $MnFe_2O_4$, also with significant OER catalytic activity, is mentioned in this paper.

Current research applications of MnO_x in electrochemistry are mainly in the direction of lithium batteries and capacitors, while in the direction of electrocatalysis, their activity is still distant from that of noble metals and transition metals such as Fe, and Ni. In this paper, while describing the current research progress, we propose the following points to further improve the electrochemical properties of MnO_x. (1) Continue to deepen the research on the catalytic mechanism of MnO_x. The mixing of multiple valence states of Mn leads to a catalytic center that is still not well defined for MnO_x, and the difference in OER activity may be due to differences in the surface electronic states of Mn^{3+}. Recent studies have proposed that the e_g orbital of Mn^{3+} is involved in the σ-bonding with the anionic adsorbent; the higher the Mn^{3+} content in the manganese group, the more favorable it is to enhance the adsorption of –OH on the catalyst surface. As a consequence, increasing the content of Mn^{3+} ions is an effective strategy to improve its OER performance. (2) On the other hand, most of the research on MnO_x has been done in alkaline environments as the Mn^{3+} ion can be unstable due to disproportionation reactions in acidic environments. However, the development of MnO_x for the OER in acidic media has made great progress and the obtained MnO_x has good catalytic properties. Therefore, we believe that the development of MnO_x in acidic media is a positive direction.

In terms of enhancing the catalytic activity of MnO_x, this can be done by introducing vacancies and forming heterogeneous interfaces. First, for the problem of insignificant catalytic activity, vacancies can activate adjacent metal sites as fresh active sites for electrocatalysis and promote the OER by synergistic interaction with Mn ions; meanwhile, the presence of a large number of oxygen vacancies in MnO_x promotes the formation of Mn^{3+} active sites, which leads to their semiconducting nature and optimizes the local electronic configuration. Second, for low conductivity, the preparation of atomic heterojunctions can effectively modulate the electronic and band structure of the catalysts to provide moderate adsorption/desorption behavior, and MnO_x can form heterojunctions that effectively prevent the recombination of electrons and holes and thus improve their conductivity. MOFs can be used as catalysts due to their tunable pore structure, high specific surface area, and multiple coordination sites, while MnO_x can be used as a metal backbone for organic structures and also as a catalyst for the OER. Finally, we propose that recombining MnO_x catalysts with other electrically active materials or conducting substrates is also an effective strategy for fabricating high-performance electrocatalysts.

In summary, the development of MnO_x materials with high stability and good catalytic properties is our objective. We believe that with the continued maturation of material preparation techniques, the gradual evolution of characterization methods, the exploration of reasonable structures, and the breakthroughs in related electrocatalytic reactions, commercial applications of MnO_x can eventually be realized.

Conflicts of interest

There are no conflicts to declare.

Acknowledgements

This work was financially supported by the National Natural Science Foundation of China (No. 51971058 and 52071072).

References

1 G. Semieniuk, L. Taylor, A. Rezai and D. K. Foley, *Nat. Clim. Change*, 2021, **11**, 313–342.
2 D. Gernaat, H. S. de Boer, V. Daioglou, S. G. Yalew, C. Muller and D. P. van Vuuren, *Nat. Clim. Change*, 2021, **11**, 362.
3 T. Yi, H. M. K. Sari, X. Li, F. Wang, Y. Zhu, J. Hu, J. Zhang and X. Li, *Nano Energy*, 2021, **85**, 105955.
4 X. Xie, L. Du, L. Yan, S. Park, Y. Qiu, J. Sokolowski, W. Wang and Y. Shao, *Adv. Funct. Mater.*, 2022, **32**, 2110036.
5 L. W. Chen and H. W. Liang, *Catal. Sci. Technol.*, 2021, **11**, 4673–4689.
6 H. J. Song, H. Yoon, B. Ju and D. W. Kim, *Adv. Energy Mater.*, 2021, **11**, 2002428.
7 W. Zhang, M. Yin, Q. Zhao, C. Jin, N. Wang, S. Ji, C. L. Ritt, M. Elimelech and Q. An, *Nat. Nanotechnol.*, 2021, **16**, 337–343.
8 Y. Zhang, F. Gao, D. Wang, Z. Li, X. Wang, C. Wang, K. Zhang and Y. Du, *Coord. Chem. Rev.*, 2023, **475**, 214916.
9 Q. Chen, N. Gong, T. Zhu, C. Yang, W. Peng, Y. Li, F. Zhang and X. Fan, *Small*, 2022, **18**, 2105696.
10 T. T. Wei, P. P. Peng, Y. R. Ji, Y. R. Zhu, T. F. Yi and Y. Xie, *J. Energy Chem.*, 2022, **71**, 400–410.
11 Y. T. Yan, J. H. Lin, J. Cao, S. Guo, X. H. Zheng, J. C. Feng and J. L. Qi, *J. Mater. Chem. A*, 2019, **7**, 24486–24492.
12 W. Shi, W. Lee and J. M. Xue, *Chemsuschem*, 2021, **14**, 1634–1658.
13 Q. Zhao, A. Song, S. Ding, R. Qin, Y. Cui, S. Li and F. Pan, *Adv. Mater.*, 2020, **32**, 2002450.
14 T. Xiong, Y. Zhang, W. S. V. Lee and J. Xue, *Adv. Energy Mater.*, 2020, **10**, 2001769.
15 F. Y. Chen, Z. Y. Wu, Z. Adler and H. T. Wang, *Joule*, 2021, **5**, 1704–1731.
16 Z. Lei, T. Wang, B. Zhao, W. Cai, Y. Liu, S. Jiao, Q. Li, R. Cao and M. Liu, *Adv. Energy Mater.*, 2020, **10**, 2000478.
17 Y. Qin, Y. Liu, Y. Zhang, Y. Gu, Y. Lian, Y. Su, J. Hu, X. Zhao, Y. Peng, K. Feng, J. Zhong, M. H. Rummeli and Z. Deng, *ACS Catal.*, 2023, **13**, 256–266.
18 J. Yu, F. Yu, M. F. Yuen and C. D. Wang, *J. Mater. Chem. A*, 2021, **9**, 9389–9430.

19 C. L. Hu, L. Zhang and J. L. Gong, *Energy Environ. Sci.*, 2019, **12**, 2620–2645.
20 Q. Liang, G. Brocks and A. Bieberle-Hütter, *JPhys Energy*, 2021, **3**, 26001.
21 J. O. Olowoyo and R. J. Kriek, *Small*, 2022, **18**, 2203125.
22 K. Zhang and R. Zou, *Small*, 2021, **17**, 2100129.
23 M. Tahir, L. Pan, F. Idrees, X. W. Zhang, L. Wang, J. J. Zou and Z. L. Wang, *Nano Energy*, 2017, **37**, 136–157.
24 H. Y. Chang, Z. J. Liang, L. Wang and C. Wang, *Nanoscale*, 2022, **14**, 5639–5656.
25 H. Dau, C. Limberg, T. Reier, M. Risch, S. Roggan and P. Strasser, *Chemcatchem*, 2010, **2**, 724–761.
26 C. X. Zhao, J. N. Liu, J. Wang, D. Ren, B. Q. Li and Q. Zhang, *Chem. Soc. Rev.*, 2021, **50**, 7745–7778.
27 Z. Y. Yu, Y. Duan, X. Y. Feng, X. X. Yu, M. R. Gao and S. H. Yu, *Adv. Mater.*, 2021, **33**, 2007100.
28 L. K. Gao, X. Cui, C. D. Sewell, J. Li and Z. Q. Lin, *Chem. Soc. Rev.*, 2021, **50**, 8428–8469.
29 Y. Zhang, C. Han, J. Gao, L. Pan, J. Wu, X. Zhu and J. Zou, *ACS Catal.*, 2021, **11**, 12485–12509.
30 Z. Xue, X. Y. Zhang, J. Q. Qin and R. P. Liu, *J. Mater. Chem. A*, 2019, **7**, 23091–23097.
31 X. W. Liu, J. J. Xu, Z. Y. Ni, R. C. Wang, J. H. You and R. Guo, *Chem. Eng. J.*, 2019, **356**, 22–33.
32 M. I. Jamesh and X. M. Sun, *J. Power Sources*, 2018, **400**, 31–68.
33 H. Osgood, S. V. Devaguptapu, H. Xu, J. Cho and G. Wu, *Nano Today*, 2016, **11**, 601–625.
34 M. M. Najafpour, M. Holynska and S. Salimi, *Coord. Chem. Rev.*, 2015, **285**, 65–75.
35 J. S. Kanady, E. Y. Tsui, M. W. Day and T. Agapie, *Science*, 2011, **333**, 733–736.
36 M. M. Najafpour, B. Haghighi, D. J. Sedigh and M. Z. Ghobadi, *Dalton Trans.*, 2013, **42**, 16683.
37 M. M. Najafpour and D. J. Sedigh, *Dalton Trans.*, 2013, **42**, 12173–12178.
38 A. Konarov, N. Voronina, J. H. Jo, Z. Bakenov, Y. K. Sun and S. T. Myung, *ACS Energy Lett.*, 2018, **3**, 2620–2640.
39 M. H. Alfaruqi, V. Mathew, J. Gim, S. Kim, J. Song, J. P. Baboo, S. H. Choi and J. Kim, *Chem. Mater.*, 2015, **27**, 3609–3620.
40 D. Wang, L. Wang, G. Liang, H. Li, Z. Liu, Z. Tang, J. Liang and C. Zhi, *ACS Nano*, 2019, **13**, 10643–10652.
41 V. B. R. Boppana, S. Yusuf, G. S. Hutchings and F. Jiao, *Adv. Funct. Mater.*, 2013, **23**, 878–884.
42 R. Yang, Y. Fan, R. Ye, Y. Tang, X. Cao, Z. Yin and Z. Zeng, *Adv. Mater.*, 2021, **33**, 2004862.
43 X. Peng, H. Y. Peng, K. N. Zhao, Y. X. Zhang, F. J. Xia, J. H. Lyu, G. Van Tendeloo, C. L. Sun and J. S. Wu, *ACS Appl. Mater. Interfaces*, 2021, **13**, 33644–33651.
44 D. M. Robinson, Y. B. Go, M. Mui, G. Gardner, Z. J. Zhang, D. Mastrogiovanni, E. Garfunkel, J. Li, M. Greenblatt and G. C. Dismukes, *J. Am. Chem. Soc.*, 2013, **135**, 3494–3501.
45 Y. T. Meng, W. Q. Song, H. Huang, Z. Ren, S. Y. Chen and S. L. Suib, *J. Am. Chem. Soc.*, 2014, **136**, 11452–11464.
46 X. Zhang, P. Yu, D. Wang and Y. Ma, *J. Nanosci. Nanotechnol.*, 2010, **10**, 898–904.
47 L. M. Housel, L. Wang, A. Abraham, J. Huang, G. D. Renderos, C. D. Quilty, A. B. Brady, A. C. Marschilok, K. J. Takeuchi and E. S. Takeuchi, *Acc. Chem. Res.*, 2018, **51**, 575–582.
48 Z. Yang, D. C. Ford, J. S. Park, Y. Ren, S. Kim, H. Kim, T. T. Fister, M. K. Y. Chan and M. M. Thackeray, *Chem. Mater.*, 2017, **29**, 1507–1517.
49 Y. Gu, G. Yan, Y. Lian, P. Qi, Q. Mu, C. Zhang, Z. Deng and Y. Peng, *Energy Storage Mater.*, 2019, **23**, 252–260.
50 Y. Zhou, Z. Zhou, L. Hu, R. Tian, Y. Wang, H. Arandiyan, F. Chen, M. Li, T. Wan, Z. Han, Z. Ma, X. Lu, C. Cazorla, T. Wu and D. Chu, *Chem. Eng. J.*, 2022, **438**, 135561.
51 S. Ni, H. Zhang, Y. Zhao, X. Li, Y. Sun, J. Qian, Q. Xu, P. Gao, D. Wu, K. Kato, M. Yamauchi and Y. Sun, *Chem. Eng. J.*, 2019, **366**, 631–638.
52 D. A. Kitchaev, S. T. Dacek, W. H. Sun and G. Ceder, *J. Am. Chem. Soc.*, 2017, **139**, 2672–2681.
53 X. C. Duan, J. Q. Yang, H. Y. Gao, J. M. Ma, L. F. Jiao and W. J. Zheng, *Crystengcomm*, 2012, **14**, 4196–4204.
54 S. L. Suib, *J. Mater. Chem.*, 2008, **18**, 1623–1631.
55 Y. Gu, Y. Min, L. Li, Y. Lian, H. Sun, D. Wang, M. H. Rummeli, J. Guo, J. Zhong, L. Xu, Y. Peng and Z. Deng, *Chem. Mater.*, 2021, **33**, 4135–4145.
56 W. Yao, G. M. Odegard, Z. Huang, Y. Yuan, H. Asayesh-Ardakani, S. Sharifi-Asl, M. Cheng, B. Song, R. Deivanayagam, F. Long, C. R. Friedrich, K. Amine, J. Lu and R. Shahbazian-Yassar, *Nano Energy*, 2018, **48**, 301–311.
57 S. Park, Y. H. Lee, S. Choi, H. Seo, M. Y. Lee, M. Balamurugan and K. T. Nam, *Energy Environ. Sci.*, 2020, **13**, 2310–2340.
58 Y. Tang, S. Zheng, S. Cao, H. Xue and H. Pang, *J. Mater. Chem. A*, 2020, **8**, 18492–18514.
59 B. Cheng, K. Kong, L. Zhang, R. Sa, T. Gu, Y. Rui and R. Wang, *Chem. Eng. J.*, 2022, **441**, 136122.
60 Z. W. Chen, M. Ju, M. Z. Sun, L. Jin, R. M. Cai, Z. Wang, L. Dong, L. M. Peng, X. Long, B. L. Huang and S. H. Yang, *Angew. Chem., Int. Ed.*, 2021, **60**, 9699–9705.
61 I. G. McKendry, L. J. Mohamad, A. C. Thenuwara, T. Marshall, E. Borguet, D. R. Strongin and M. J. Zdilla, *ACS Energy Lett.*, 2018, **3**, 2280–2285.
62 Y. Y. Pu, M. J. Lawrence, V. Celorrio, Q. Wang, M. Gu, Z. Z. Sun, L. A. Jacome, A. E. Russell, L. M. Huang and P. Rodriguez, *J. Mater. Chem. A*, 2020, **8**, 13340–13350.
63 G. Gupta, K. Selvakumar, N. Lakshminarasimhan, S. Kumar and M. Mamlouk, *J. Power Sources*, 2020, **461**, 228131.
64 X. F. Lu, A. L. Wang, H. Xu, X. J. He, Y. X. Tong and G. R. Li, *J. Mater. Chem. A*, 2015, **3**, 16560–16566.
65 X. F. Lu, Z. X. Huang, Y. X. Tong and G. R. Li, *Chem. Sci.*, 2016, **7**, 510–517.
66 N. N. Xu, J. W. Liu, J. L. Qiao, H. T. Huang and X. D. Zhou, *J. Power Sources*, 2020, **455**, 227992.
67 B. Z. Jiang, C. J. Xu, C. L. Wu, L. B. Dong, J. Li and F. Y. Kang, *Electrochim. Acta*, 2017, **229**, 422–428.
68 M. Mao, X. X. Wu, Y. Hu, Q. H. Yuan, Y. B. He and F. Y. Kang, *J. Energy Chem.*, 2021, **52**, 277–283.
69 N. Parveen, S. A. Ansari, M. Z. Ansari and M. O. Ansari, *Environ. Chem. Lett.*, 2022, **20**, 283–309.

70 S. E. Balaghi, C. A. Triana and G. R. Patzke, *ACS Catal.*, 2020, **10**, 2074–2087.
71 P. Liu, Y. Zheng, H. Zhu and T. Li, *ACS Appl. Nano Mater.*, 2019, **2**, 744–749.
72 G. Zhao, Y. Yao, W. Lu, G. Liu, X. Guo, A. Tricoli and Y. Zhu, *Nano Lett.*, 2021, **21**, 7012–7020.
73 L. Bigiani, C. Maccato, T. Andreu, A. Gasparotto, C. Sada, E. Modin, O. I. Lebedev, J. R. Morante and D. Barreca, *ACS Appl. Nano Mater.*, 2020, **3**, 9889–9898.
74 K. R. Yoon, G. Y. Lee, J. W. Jung, N. H. Kim, S. O. Kim and I. D. Kim, *Nano Lett.*, 2016, **16**, 2076–2083.
75 B. Yang, X. Chang, X. Y. Ding, X. Z. Ma and M. Y. Zhang, *J. Colloid Interface Sci.*, 2022, **623**, 196–204.
76 P. R. Garcês Gonçalves, H. A. De Abreu and H. A. Duarte, *J. Phys. Chem. C*, 2018, **122**, 20841–20849.
77 Y. Shi, P. F. Ndione, L. Y. Lim, D. Sokaras, T. Weng, A. R. Nagaraja, A. G. Karydas, J. D. Perkins, T. O. Mason, D. S. Ginley, A. Zunger and M. F. Toney, *Chem. Mater.*, 2014, **26**, 1867–1873.
78 C. Chowde Gowda, A. Mathur, A. Parui, P. Kumbhakar, P. Pandey, S. Sharma, A. Chandra, A. K. Singh, A. Halder and C. S. Tiwary, *Ind. Eng. Chem.*, 2022, **113**, 153–160.
79 Y. Gorlin, B. Lassalle-Kaiser, J. D. Benck, S. Gul, S. M. Webb, V. K. Yachandra, J. Yano and T. F. Jaramillo, *J. Am. Chem. Soc.*, 2013, **135**, 8525–8534.
80 M. Huynh, C. Shi, S. J. L. Billinge and D. G. Nocera, *J. Am. Chem. Soc.*, 2015, **137**, 14887–14904.
81 C. Guo, Y. Zheng, J. Ran, F. Xie, M. Jaroniec and S. Z. Qiao, *Angew. Chem., Int. Ed.*, 2017, **56**, 8539–8543.
82 F. B. Wang, G. D. Li, X. G. Meng, S. J. Xu and W. Q. Ma, *J. Power Sources*, 2020, **462**, 228162.
83 Q. Huang, X. Zhong, Q. Zhang, X. Wu, M. Jiao, B. Chen, J. Sheng and G. Zhou, *J. Energy Chem.*, 2022, **68**, 679–687.
84 J. S. Hong, H. Seo, Y. H. Lee, K. H. Cho, C. Ko, S. Park and K. T. Nam, *Small Methods*, 2020, **4**, 1900733.
85 K. H. Cho, H. Seo, S. Park, Y. H. Lee, M. Y. Lee, N. H. Cho and K. T. Nam, *Adv. Funct. Mater.*, 2020, **30**, 1910424.
86 M. Y. Lee, H. Ha, K. H. Cho, H. Seo, S. Park, Y. H. Lee, S. J. Kwon, T. W. Lee and K. T. Nam, *ACS Catal.*, 2020, **10**, 1237–1245.
87 J. Kim, J. Lee, C. Liu, S. Pandey, S. Woo Joo, N. Son and M. Kang, *Appl. Surf. Sci.*, 2021, **546**, 149124.
88 D. Zhang, J. Cao, X. Zhang, N. Insin, S. Wang, J. Han, Y. Zhao, J. Qin and Y. Huang, *Adv. Funct. Mater.*, 2021, **31**, 2009412.
89 Q. Tan, X. Li, B. Zhang, X. Chen, Y. Tian, H. Wan, L. Zhang, L. Miao, C. Wang, Y. Gan, J. Jiang, Y. Wang and H. Wang, *Adv. Energy Mater.*, 2020, **10**, 2001050.
90 M. Augustin, O. Yezerska, D. Fenske, I. Bardenhagen, A. Westphal, M. Knipper, T. Plaggenborg, J. Kolny-Olesiak and J. Parisi, *Electrochim. Acta*, 2015, **158**, 383–389.
91 R. Pokhrel, M. K. Goetz, S. E. Shaner, X. X. Wu and S. S. Stahl, *J. Am. Chem. Soc.*, 2015, **137**, 8384–8387.
92 J. M. Lee, S. B. Patil, B. Kang, S. Lee, M. G. Kim and S. J. Hwang, *J. Mater. Chem. A*, 2018, **6**, 12565–12573.
93 H. Li, W. Zhang, K. Sun, J. Guo, K. Yuan, J. Fu, T. Zhang, X. Zhang, H. Long, Z. Zhang, Y. Lai and H. Sun, *Adv. Energy Mater.*, 2021, **11**, 2100867.
94 K. Jin, H. Seo, T. Hayashi, M. Balamurugan, D. Jeong, Y. K. Go, J. S. Hong, K. H. Cho, H. Kakizaki, N. Bonnet-Mercier, M. G. Kim, S. H. Kim, R. Nakamura and K. T. Nam, *J. Am. Chem. Soc.*, 2017, **139**, 2277–2285.
95 Y. Tong, Y. Q. Guo, P. Z. Chen, H. F. Liu, M. X. Zhang, L. D. Zhang, W. S. Yan, W. S. Chu, C. Z. Wu and Y. Xie, *Chem*, 2017, **3**, 812–821.
96 H. Y. An, Z. Chen, J. X. Yang, Z. C. Feng, X. L. Wang, F. T. Fan and C. Li, *J. Catal.*, 2018, **367**, 53–61.
97 B. Kang, X. Jin, S. M. Oh, S. B. Patila, M. G. Kim, S. H. Kim and S. J. Hwang, *Appl. Catal., B*, 2018, **236**, 107–116.
98 F. Yang, J. Xie, D. Rao, X. Liu, J. Jiang and X. Lu, *Nano Energy*, 2021, **85**, 106020.
99 P. Plate, C. Höhn, U. Bloeck, P. Bogdanoff, S. Fiechter, F. F. Abdi, R. van de Krol and A. C. Bronneberg, *ACS Appl. Mater. Interfaces*, 2021, **13**, 2428–2436.
100 H. Feizi, S. M. Hosseini, Z. Zand and M. M. Najafpour, *J. Hydrogen Energy*, 2022, **47**, 7813–7822.
101 T. Takashima, K. Hashimoto and R. Nakamura, *J. Am. Chem. Soc.*, 2012, **134**, 18153–18156.
102 J. Park, H. Kim, K. Jin, B. J. Lee, Y. S. Park, H. Kim, I. Park, K. D. Yang, H. Y. Jeong, J. Kim, K. T. Hong, H. W. Jang, K. Kang and K. T. Nam, *J. Am. Chem. Soc.*, 2014, **136**, 4201–4211.
103 J. Lu, H. Wang, Y. Sun, X. Wang, X. Song and R. Wang, *Chem. Eng. J.*, 2021, **417**, 127894.
104 H. Kakizaki, H. Ooka, T. Hayashi, A. Yamaguchi, N. Bonnet Mercier, K. Hashimoto and R. Nakamura, *Adv. Funct. Mater.*, 2018, **28**, 1706319.
105 Z. M. Chan, D. A. Kitchaev, J. N. Weker, C. Schnedermann, K. Lim, G. Ceder, W. Tumas, M. F. Toney and D. G. Nocera, *Proc. Natl. Acad. Sci. U. S. A.*, 2018, **115**, E5261–E5268.
106 C. Wei, Z. Feng, G. G. Scherer, J. Barber, Y. Shao-Horn and Z. J. Xu, *Adv. Mater.*, 2017, **29**, 1606800.
107 T. Takashima, K. Hashimoto and R. Nakamura, *J. Am. Chem. Soc.*, 2012, **134**, 1519–1527.
108 M. Huynh, D. K. Bediako and D. G. Nocera, *J. Am. Chem. Soc.*, 2014, **136**, 6002–6010.
109 K. X. Wang, Y. L. Wang, B. Yang, Z. J. Li, X. T. Qin, Q. H. Zhang, L. C. Lei, M. Qiu, G. Wu and Y. Hou, *Energy Environ. Sci.*, 2022, **15**, 2356–2365.
110 H. Xue, A. Meng, T. Yang, Z. Li and C. Chen, *J. Energy Chem.*, 2022, **71**, 639–651.
111 K. Ham, S. Hong, S. Kang, K. Cho and J. Lee, *ACS Energy Lett.*, 2021, **6**, 364–370.
112 Y. Yan, P. Wang, J. Lin, J. Cao and J. Qi, *J. Energy Chem.*, 2021, **58**, 446–462.
113 Y. Yan, J. Lin, T. Xu, B. Liu, K. Huang, L. Qiao, S. Liu, J. Cao, S. C. Jun, Y. Yamauchi and J. Qi, *Adv. Energy Mater.*, 2022, **12**, 2200434.
114 Y. Zhao, C. Chang, F. Teng, Y. Zhao, G. Chen, R. Shi, G. I. N. Waterhouse, W. Huang and T. Zhang, *Adv. Energy Mater.*, 2017, **7**, 1700005.

115 Y. Liu, H. T. D. Bui, A. R. Jadhav, T. Yang, S. Saqlain, Y. Luo, J. Yu, A. Kumar, H. Wang, L. Wang, V. Q. Bui, M. G. Kim, Y. D. Kim and H. Lee, *Adv. Funct. Mater.*, 2021, **31**, 2010718.
116 Z. Zhang, H. Sun, J. Li, Z. Shi, M. Fan, H. Bian, T. Wang and D. Gao, *J. Power Sources*, 2021, **491**, 229584.
117 Q. C. Xu, J. H. Zhang, H. X. Zhang, L. Y. Zhang, L. Chen, Y. J. Hu, H. Jiang and C. Z. Li, *Energy Environ. Sci.*, 2021, **14**, 5228–5259.
118 Z. X. Li, M. L. Hu, P. Wang, J. H. Liu, J. S. Yao and C. Y. Li, *Coord. Chem. Rev.*, 2021, **439**, 213953.
119 J. Zhu, M. Sun, S. J. Liu, X. H. Liu, K. Hu and L. Wang, *J. Mater. Chem. A*, 2019, **7**, 26975–26983.
120 P. Wang, Y. Luo, G. Zhang, Z. Chen, H. Ranganathan, S. Sun and Z. Shi, *Nano-Micro Lett.*, 2022, **14**, 117–120.
121 Y. L. Niu, X. Teng, S. Q. Gong, X. Liu, M. Z. Xu and Z. F. Chen, *Energy Storage Mater.*, 2021, **43**, 42–52.
122 T. Meng and M. H. Cao, *ACS Sustainable Chem. Eng.*, 2020, **8**, 13271–13281.
123 F. Li, T. T. Qin, Y. P. Sun, R. J. Jiang, J. F. Yuan, X. Q. Liu and A. P. O'Mullane, *J. Mater. Chem. A*, 2021, **9**, 22533–22543.
124 S. S. Selvasundarasekar, T. K. Bijoy, S. Kumaravel, A. Karmakar, R. Madhu, K. Bera, S. Nagappan, H. N. Dhandapani, G. A. M. Mersal, M. M. Ibrahim, D. Sarkar, S. M. Yusuf, S. Lee and S. Kundu, *ACS Appl. Mater. Interfaces*, 2022, **14**, 46581–46594.
125 S. Wu, H. Min, W. Shi and P. Cheng, *Adv. Mater.*, 2019, **32**, 1805871.
126 B. Li, J. Ma and P. Cheng, *Angew. Chem., Int. Ed.*, 2018, **57**, 6834–6837.
127 J. Wang, J. Wang, M. Zhang, S. Li, R. Liu and Z. Li, *J. Alloys Compd.*, 2020, **821**, 153463.
128 X. Wei, S. Cao, H. Xu, C. Jiang, Z. Wang, Y. Ouyang, X. Lu, F. Dai and D. Sun, *ACS Mater. Lett.*, 2022, **4**, 1991–1998.
129 T. F. Yi, L. Y. Qiu, J. Mei, S. Y. Qi, P. Cui, S. H. Luo, Y. R. Zhu, Y. Xie and Y. B. He, *Sci. Bull.*, 2020, **65**, 546–556.
130 Y. Chen, Y. Guo, H. Cui, Z. Xie, X. Zhang, J. Wei and Z. Zhou, *J. Mater. Chem. A*, 2018, **6**, 9716–9722.
131 F. Wang, H. Zhao, Y. Ma, Y. Yang, B. Li, Y. Cui, Z. Guo and L. Wang, *J. Energy Chem.*, 2020, **50**, 52–62.
132 C. Chen, Z. J. Tang, J. Y. Li, C. Y. Du, T. Ouyang, K. Xiao and Z. Q. Liu, *Adv. Funct. Mater.*, 2023, **33**, 2210143.
133 B. Liu, Y. Sun, L. Liu, S. Xu and X. Yan, *Adv. Funct. Mater.*, 2018, **28**, 1704973.
134 Y. W. Li, S. K. Su, C. Z. Yue, J. Shu, P. F. Zhang, F. H. Du, S. N. Wang, H. Y. Ma, J. Yin and X. Shao, *Dalton Trans.*, 2021, **50**, 17265–17274.
135 R. Guo, A. Yan, J. Xu, B. Xu, T. Li, X. Liu, T. Yi and S. Luo, *J. Alloys Compd.*, 2020, **817**, 153246.
136 K. H. Cho, H. Seo, S. Park, Y. H. Lee, M. Y. Lee, N. H. Cho and K. T. Nam, *Adv. Funct. Mater.*, 2020, **30**, 1910424.
137 Y. T. Yan, J. Q. Liu, K. K. Huang, J. L. Qi, L. Qiao, X. H. Zheng and W. Cai, *J. Mater. Chem. A*, 2021, **9**, 26777–26787.
138 J. Qi, Y. Yan, Y. Cai, J. Cao and J. Feng, *Adv. Funct. Mater.*, 2021, **31**, 2006030.
139 Y. Lin, G. Yang, Y. Fu, B. Zhu, J. Zhao and J. Li, *J. Phys. Chem. Solids*, 2022, **160**, 110373.
140 X. Chang, B. Yang, X. Ding, X. Ma and M. Zhang, *J. Colloid Interface Sci.*, 2022, **610**, 663–670.
141 S. Chen, Y. Huang, M. Li, P. Sun, X. Lv, B. Li, L. Fang and X. Sun, *J. Electroanal. Chem.*, 2021, **895**, 115513.
142 Y. D. Xue, Z. S. Fishman, J. A. Rohr, Z. H. Pan, Y. T. Wang, C. H. Zhang, S. L. Zheng, Y. Zhang and S. Hu, *J. Mater. Chem. A*, 2018, **6**, 21918–21926.
143 Z. Wang, C. Wang, L. Ye, X. Liu, L. Xin, Y. Yang, L. Wang, W. Hou, Y. Wen and T. Zhan, *Inorg. Chem.*, 2022, **61**, 15256–15265.
144 Y. W. Li, S. K. Su, C. Z. Yue, J. Shu, P. F. Zhang, F. H. Du, S. N. Wang, H. Y. Ma, J. Yin and X. Shao, *Dalton Trans.*, 2021, **50**, 17265–17274.
145 P. Wang, Y. Luo, G. Zhang, M. Wu, Z. Chen, S. Sun and Z. Shi, *Small*, 2022, **18**, 2105803.
146 W. Zhang, L. Zong, K. Fan, L. Cui, Q. Zhang, J. Zhao, L. Wang and S. Feng, *J. Alloys Compd.*, 2021, **874**, 159965.
147 X. F. Lu, Y. Chen, S. Wang, S. Gao and X. W. D. Lou, *Adv. Mater.*, 2019, **31**, 1902339.
148 W. Wang, H. Wang, Z. Wu, Y. Yu, M. Asif, Z. Wang, X. Qiu and H. Liu, *Electrochim. Acta*, 2018, **281**, 486–493.
149 W. Q. Li, H. Q. Fu, Y. H. Cao, H. J. Wang, H. Yu, Z. W. Qiao, H. Liang and F. Peng, *Chemelectrochem*, 2019, **6**, 359–368.
150 R. Dong, A. Zhu, W. Zeng, L. Qiao, L. Lu, Y. Liu, P. Tan and J. Pan, *Appl. Surf. Sci.*, 2021, **544**, 148860.
151 J. Kim, J. Lee, C. Liu, S. Pandey, S. Woo Joo, N. Son and M. Kang, *Appl. Surf. Sci.*, 2021, **546**, 149124.
152 F. Wang, G. Li, X. Meng, S. Xu and W. Ma, *J. Power Sources*, 2020, **462**, 228162.
153 Q. Huang, X. Zhong, Q. Zhang, X. Wu, M. Jiao, B. Chen, J. Sheng and G. Zhou, *J. Energy Chem.*, 2022, **68**, 679–687.
154 S. Niu, X. Kong, S. Li, Y. Zhang, J. Wu, W. Zhao and P. Xu, *Appl. Catal., B*, 2021, **297**, 120442.
155 X. Zhai, X. Wang, X. Pang, J. Zhang, Q. Wu, W. Na, Y. Zhou and L. Tian, *J. Taiwan Inst. Chem. Eng.*, 2021, **126**, 383–391.
156 C. Deng, K. Wu, J. Scott, S. Zhu, R. Amal and D. Wang, *J. Mater. Chem. A*, 2019, **7**, 20649–20657.
157 C. Zhang, F. Kong, Y. Qiao, Q. Zhao, A. Kong and Y. Shan, *Chem. - Asian J.*, 2020, **15**, 3535–3541.
158 T. Meng, B. Mao and M. Cao, *Inorg. Chem.*, 2021, **60**, 10340–10349.

